ELEMENTA
Science of the Anthropocene

Cole, ST, et al 2017 Ice and ocean velocity in the Arctic marginal ice zone: Ice roughness and momentum transfer. *Elem Sci Anth,* 5: 55, DOI: https://doi.org/10.1525/elementa.241

RESEARCH ARTICLE

Ice and ocean velocity in the Arctic marginal ice zone: Ice roughness and momentum transfer

Sylvia T. Cole[*], John M. Toole[*], Ratnaksha Lele[*], Mary-Louise Timmermans[†], Shawn G. Gallaher[‡], Timothy P. Stanton[§], William J. Shaw[§], Byongjun Hwang[‖], Ted Maksym[*], Jeremy P. Wilkinson[¶], Macarena Ortiz[**], Hans Graber[**], Luc Rainville[††], Alek A. Petty[‡‡], Sinéad L. Farrell[‡‡], Jackie A. Richter-Menge[§§] and Christian Haas[‖‖]

The interplay between sea ice concentration, sea ice roughness, ocean stratification, and momentum transfer to the ice and ocean is subject to seasonal and decadal variations that are crucial to understanding the present and future air-ice-ocean system in the Arctic. In this study, continuous observations in the Canada Basin from March through December 2014 were used to investigate spatial differences and temporal changes in under-ice roughness and momentum transfer as the ice cover evolved seasonally. Observations of wind, ice, and ocean properties from four clusters of drifting instrument systems were complemented by direct drill-hole measurements and instrumented overhead flights by NASA operation IceBridge in March, as well as satellite remote sensing imagery about the instrument clusters. Spatially, directly estimated ice-ocean drag coefficients varied by a factor of three with rougher ice associated with smaller multi-year ice floe sizes embedded within the first-year-ice/multi-year-ice conglomerate. Temporal differences in the ice-ocean drag coefficient of 20–30% were observed prior to the mixed layer shoaling in summer and were associated with ice concentrations falling below 100%. The ice-ocean drag coefficient parameterization was found to be invalid in September with low ice concentrations and small ice floe sizes. Maximum momentum transfer to the ice occurred for moderate ice concentrations, and transfer to the ocean for the lowest ice concentrations and shallowest stratification. Wind work and ocean work on the ice were the dominant terms in the kinetic energy budget of the ice throughout the melt season, consistent with free drift conditions. Overall, ice topography, ice concentration, and the shallow summer mixed layer all influenced mixed layer currents and the transfer of momentum within the air-ice-ocean system. The observed changes in momentum transfer show that care must be taken to determine appropriate parameterizations of momentum transfer, and imply that the future Arctic system could become increasingly seasonal.

Keywords: Arctic ocean; ice-ocean boundary layer; momentum transfer

1. Introduction

The canonical view of subinertial ocean currents immediately beneath sea ice consists of a logarithmic boundary layer, within which the stress is independent of depth, and an Ekman layer, where the influence of the Earth's rotation becomes important (**Figure 1**; McPhee, 2008). Together these layers are termed the ice-ocean boundary layer (IOBL), and encompass the upper tens of meters of the Arctic Ocean. The logarithmic boundary layer is typically a few meters thick at most, but within it currents vary logarithmically with depth. The Ekman layer under sea ice has currents that decay and rotate with depth. The specific details

* Woods Hole Oceanographic Institution, Woods Hole, Massachusetts, US
† Yale University, New Haven, Connecticut, US
‡ United States Naval Academy, Annapolis, Maryland, US
§ Naval Postgraduate School, Monterey, California, US
‖ Scottish Association for Marine Science, Oban, GB
¶ British Antarctic Survey, Cambridge, GB
** RSMAS, University of Miami, Miami, Florida, US
†† Applied Physics Laboratory, University of Washington, Seattle, Washington, US
‡‡ Earth System Science Interdisciplinary Center, University of Maryland, College Park, Maryland, US
§§ Cold Regions Research and Engineering Laboratory, Hanover, New Hampshire, US
‖‖ York University, Toronto, Ontario, CA
Corresponding author: Sylvia T. Cole (scole@whoi.edu)

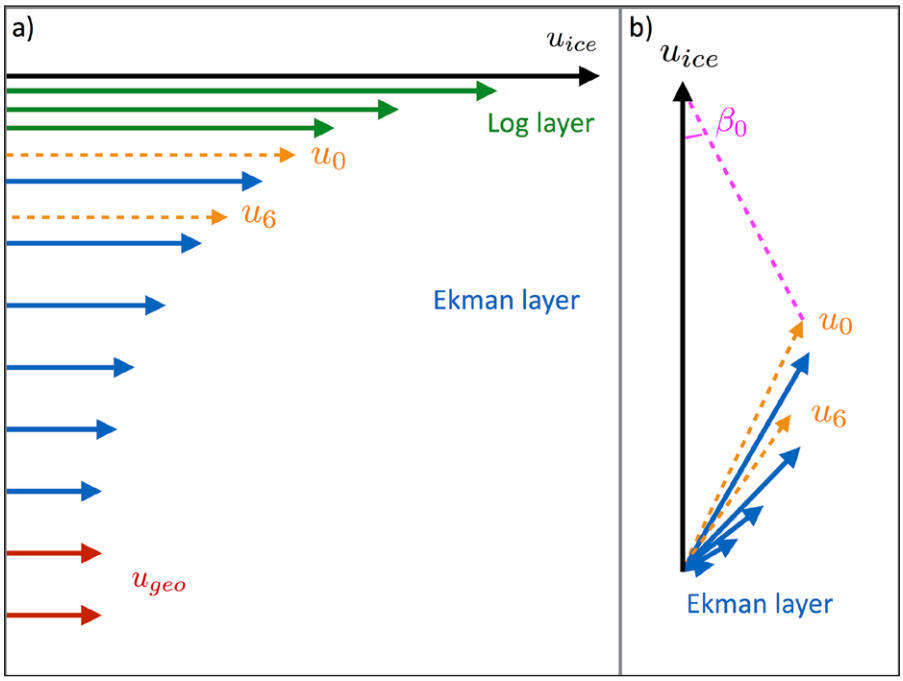

Figure 1: Schematic of ice and upper ocean currents. a) A profile view, and **b)** a top-down view using the geostrophic current as the reference velocity. The velocity at the interface between the logarithmic boundary layer and Ekman layer (u_0) and a representative measurement depth for winter conditions (u_6) are shown, as is the turning angle of the ice-ocean drag coefficient, β_0. DOI: https://doi.org/10.1525/elementa.241.f1

of these layers (e.g., layer thicknesses, current speed variations with depth, rate of turning, etc.) are affected directly by the stratification in the upper tens of meters and the intensity of upper ocean turbulence, which is influenced by several factors including the ice speed, roughness and concentration. All of these parameters are changing on decadal scales in the Arctic; ice speeds are increasing, the ice cover is becoming thinner and younger, ice concentrations less than 100% extend over a larger fraction of the year, and stratification is increasing (Kwok et al., 2009; Comiso, 2012; Cavalieri and Parkinson, 2012; McPhee, 2012; Kwok et al., 2013; Peralta-Ferriz and Woodgate, 2015). In addition, these parameters also change seasonally; significant ice melt, growth, ridging, and breakup alters ice speed, roughness, and concentration while air-sea heat exchange, ice melt and growth, and ice-ocean shear influence upper ocean stratification. Untangling the effects of changes in ice speed, ice roughness, ice concentration and stratification on the upper ocean currents is necessary for understanding and modeling the air-ice-ocean system on daily to decadal timescales.

The transfer of momentum within the air-ice-ocean system can be parameterized in a number of ways. One of the simplest and most frequently used approaches is to employ quadratic drag relations scaled by air-ice and ice-ocean drag coefficients. Such drag coefficients are frequently treated as constant in space and time, with thin ice, thick ice, and ice concentrations from full ice cover down to 1% being parameterized identically. However, observations of the air-ice drag coefficient show increased values for rougher ice types and within the marginal ice zone (Overland, 1985; Anderson, 1987; Guest and Davidson, 1987; Guest and Davidson, 1991; Castellani et al., 2014). Similarly, a range of values for the ice-ocean drag coefficient has been documented with rougher under-ice topography corresponding to higher ice-ocean drag coefficients (summarized in Shirasawa and Ingram, 1991 and Lu et al., 2011; see also McPhee, 2012; Martin et al., 2016). Melt conditions and partial ice concentration further complicate ice-ocean drag: form drag from floe edges is theorized to increase ice-ocean drag for small floes (Lu et al., 2011; Tsamados et al., 2014), while melt from below physically smooths the block-like structure of existing ridges, and the presence of thin "slippery" mixed layers can effectively decouple the ice and ocean in summer (Kudryavtsev and Soloviev, 1990; McPhee, 2012), both resulting in decreased ice-ocean drag coefficients. Other parameterization schemes allow the ice-ocean drag coefficient to vary (see McPhee 2008, 2012) or rely on a physical ice roughness length scale that does not vary with some parameters (e.g., ice speed or stratification; Shaw et al., 2008; McPhee, 2012). The seasonal (and decadal) changes in melting, ridging, and ice concentration alter ice-ocean drag coefficients and ice roughness lengths. Together with changes in stratification, these processes combine to alter the characteristics of wind-driven ocean currents on seasonal (and decadal) timescales.

Simultaneous observations of ocean currents and stratification within the upper tens of meters in the Arctic Ocean are rarely obtained over a full seasonal cycle. Mooring observations are necessarily subsurface and so do not observe the stratification in the upper tens of meters. Drifting platforms are typically used to observe the IOBL and upper ocean. A handful of manned drifts from several months to a year in duration have been conducted from thick multi-year ice (McPhee, 1978; Maykut and McPhee,

1995; McPhee, 2002; Pinkel, 2005), whereas short-term process studies are typically used to study environments characterized by low ice concentrations and/or thin ice (Johannessen et al., 1983; Sundfjord et al., 2007; Fer and Sundfjord, 2007; Fer et al., 2010; Sirevaag et al., 2011; Randelhoff et al., 2014). Seasonal timescale observations have been obtained from autonomous drifting platforms, but these instrument systems often do not sample the entire IOBL or its currents as well as its stratification (e.g., Shaw et al., 2008; Toole et al., 2011). Advances in observing platforms and increased focus on thinner ice and low ice concentrations, of which this study is one example, are changing this situation.

In this study, we examined ocean currents within the IOBL, ice-ocean drag, and other indicators of momentum transfer on daily to seasonal timescales. Observations were taken during the Marginal Ice Zone (MIZ) Experiment, which observed various aspects of the air-ice-ocean system from March 2014 into early 2015 (Lee et al., 2012). The MIZ experiment deployed a north-south array of drifting instruments in the eastern Canada Basin (**Figure 2**) that included sensors to observe air, ice, and ocean conditions (**Figure 3**) as the ice concentration decreased seasonally from 100% to near 0% (**Figure 4a**). The focus of this paper is on daily averaged velocities; a companion paper addresses near-inertial motions in the ice and ocean, including internal wave dynamics. The results presented here consist of a characterization of the air-ice-ocean system, the seasonal cycle of the ice-ocean drag coefficient and other indicators of momentum transfer (including upper ice surface topography), an investigation of under-ice roughness and Rossby similarity, and the kinetic energy budget of the ice.

2. Data

The bulk of the observations analyzed here derive from drifting platforms deployed as clusters of complimentary instruments (**Figure 2b**). Each cluster consisted of several sensor systems deployed within tens of meters of each other, bracketed by additional instrumentation at each of four corners located ~5 km from each other (**Figure 2c**). The data from each drifting platform are described first, followed by a description of the IceBridge and drill-hole data at cluster 2, and the remote sensing observations utilized in this analysis. We focus here on observations at clusters 2–5 (C2 through C5); cluster 1 is omitted as it did not include observations of ocean velocity.

2.1 Drifting platforms

Clusters 2–4 were deployed over a 10 day period in March 2014 from aircraft-supported ice camps spanning 73.4–75.4°N along 135°W (**Figure 2b**). The clusters drifted anticyclonically south and west through the Canada Basin such that by mid-July they were distributed more across longitude than latitude with C2 traveling the farthest west. Instrument systems ceased sampling at various times (**Figure 3**) and for various reasons (see below); here we focus principally on the March – September observations from these three clusters. Cluster 5 was deployed in August from the *R/V Araon* further to the north to provide observations in a contrasting ice concentration domain. Cluster 5 operated in the central Canada Basin through to spring 2015; only C5 observations through December 2014 are discussed here.

2.1.1 Ocean observations

Ocean currents (u, v, w; Appendix A), temperature, and salinity were observed using an instrument termed the Ice-Tethered Profiler with Velocity (ITP-V; Williams et al., 2010; Cole et al., 2014), a variant of the Ice-Tethered Profiler (Krishfield et al., 2008a) that included a velocity sensor in addition to a CTD. The surface buoy is moored into the ice, and drifts with the ice cover or ocean currents in the absence of ice (the system floats in open water) with GPS positions obtained every hour. A weighted wire extends below the surface buoy along which a profiling package crawls nominally at 0.25 m s^{-1}. Ocean velocity is estimated using a customized Nobska Inc. Modular

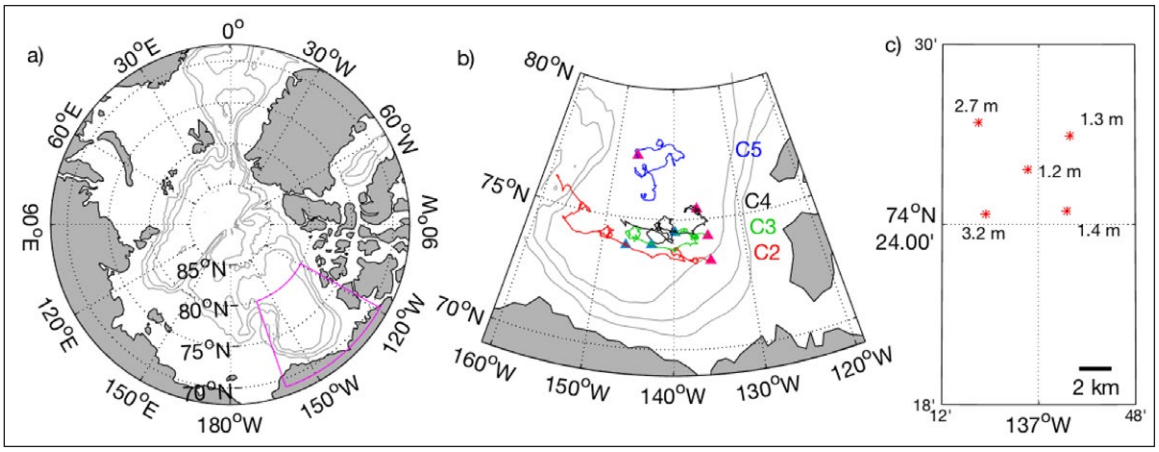

Figure 2: Map of cluster and instrument locations. a) Map of the Arctic Ocean with the 1000, 2000, and 3000-m bathymetry contours shown. Magenta box shows the region displayed in (b). **b)** Map of C2–C5 ITP-V drift tracks in 2014. Deployment locations (magenta triangles) and locations on 27 June 2014 (blue triangles) are shown. Bathymetry contours as in (a). **c)** Map of C3 IMBs on 21 March 2014 with ice draft measurements indicated. The ITP-V, AOFB, and AWS are co-located with the central IMB. DOI: https://doi.org/10.1525/elementa.241.f2

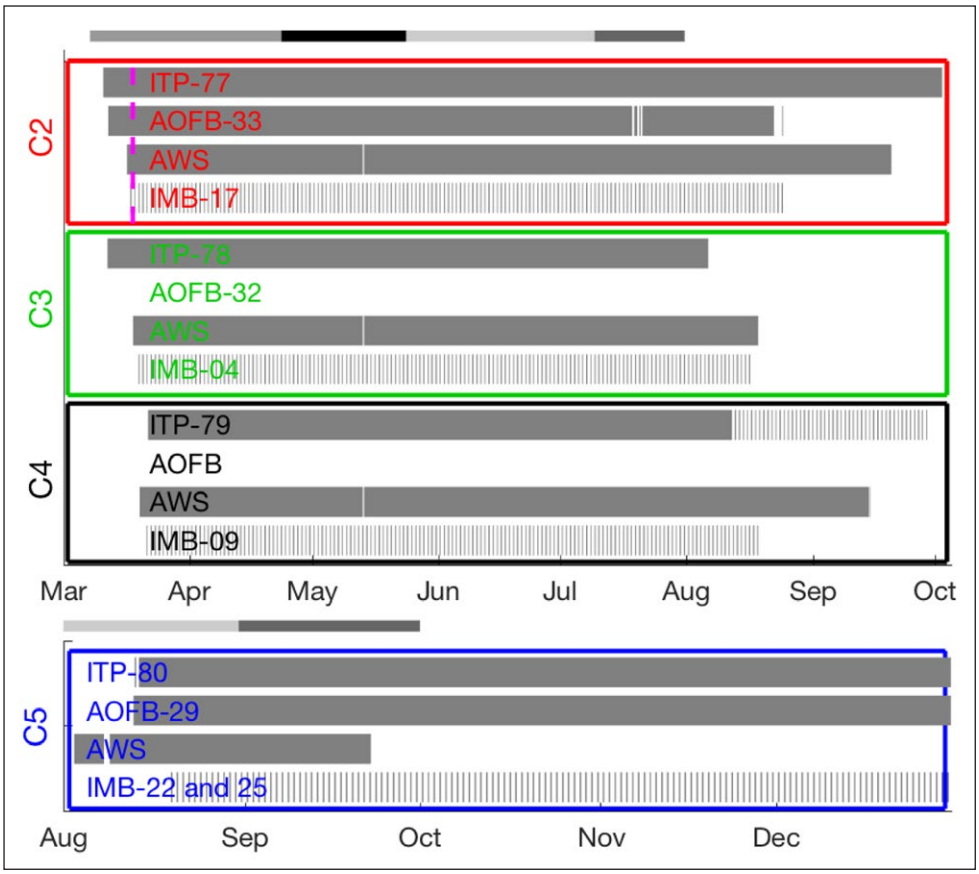

Figure 3: Time series of observations by platform and instrument cluster. C2 (red), C3 (green), C4 (black), and C5 (blue) showing ITP-V (utilizing momentum flux, ice and ocean velocity), AOFB (utilizing momentum flux), AWS (utilizing wind velocity), and IMB (utilizing ice thickness and draft) data. Dashed magenta line shows the time of the IceBridge observations at C2. The IMB time series are shown as a daily record and for the central IMB only, except for C5 which shows two of the outlying IMBs (see text). Gray bars (above C2 and C5) indicate the four time periods considered in subsequent analyses; the gray bars above C5 show only the latter two time periods. DOI: https://doi.org/10.1525/elementa.241.f3

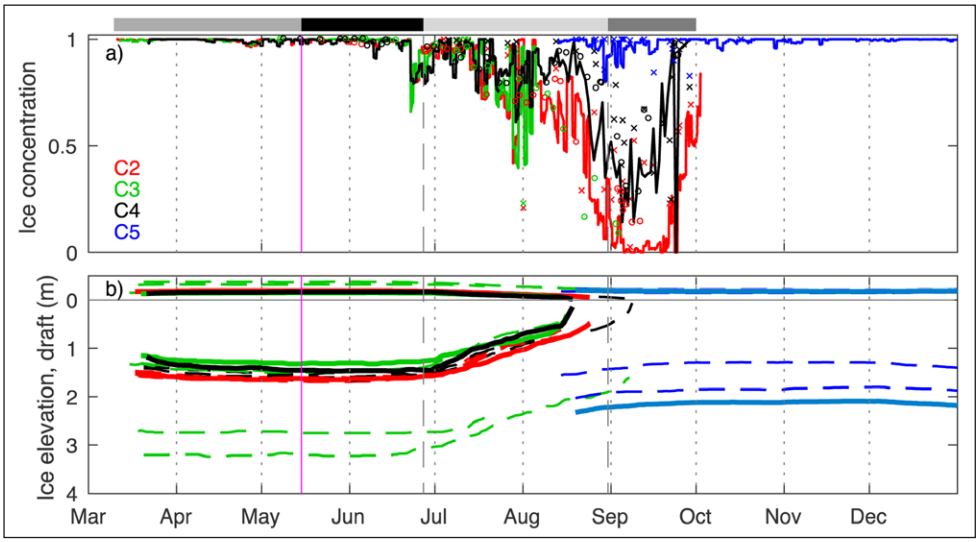

Figure 4: Ice concentration and ice thickness time series. a) Ice concentration from AMSR2 (lines), TerraSAR-X (circles), and RADARSAT-2 (Xs). RADARSAT-2 concentrations are only shown for July – September for simplicity. **b)** Ice thickness plotted as ice elevation and ice draft at C2–C5 with the central location in bold and outlying IMB data in lighter dashed lines. At C5, the lighter blue central location is the average melt/growth of the outlying IMB data combined with the initial thickness of the ITP-V hole. Gray bars as in Figure 3. Vertical magenta and dashed gray lines denote 15 May, 27 June, and 1 September. DOI: https://doi.org/10.1525/elementa.241.f4

Acoustic Velocity Sensor (MAVS) together with an inertial measurement unit (Thwaites and Krishfield, 2013). One-way profiles of *u, v*, temperature, and salinity between 7 m and 250 m were collected every 3 hours, with two profiles every other day extending to 750 m depth. In addition, 3–4 times per day between profile operations the profiler package was parked at ~6.5 m depth and sampled for 20 minutes at 1 Hz. The specific depth varied slightly (79% of fixed depth records were shallower than 8 m) with records occasionally occurring below 10 m depth (12% of fixed depth records), primarily in September, when ice speeds were fast, wire angles were large, and the profiler was unable to travel up and/or hold position at the top of its tether. The turbulent fluctuations of *T, S, u*, *v* and *w* during these fixed-depth measurement periods were used for direct covariance estimates of the turbulent heat, salt, and momentum fluxes. Details of the velocity processing and flux estimation procedures are in Cole et al. (2015) with minor updates in Appendix B. A discussion of errors in estimated ocean velocity is also included in Cole et al. (2015); pre-deployment and post-deployment calibration parameters were derived to optimize horizontal velocity accuracy while profiling (i.e., no systematic biases between upward versus downward profiles, or systematic dependence on wire angle). Temperature and salinity were produced from CTD data following Krishfield et al. (2008b).

ITP-Vs were deployed at C2 (ITP-77), C3 (ITP-78), C4 (ITP-79), and C5 (ITP-80). Due to a software problem, data telemetry at C2 ceased on 5 August and at C3, on 6 August 2014. The sampling plan for C4 was changed to one 750 m profile per day on 12 August (**Figure 3**) in anticipation of the same software problem. Although unable to telemeter, data continued to be archived aboard the profiling vehicles. Full resolution data were recovered from ITP-77 at C2 when it was recovered on 1 October (ITP-79 at C4 was also recovered on 29 September but no additional data were obtained owing to the sampling program change); ITP-78 was not recovered. ITP-80 at C5 was deployed on 13 August 2014, and telemetered data until 24 May 2015.

Arctic Ocean Flux Buoys (AOFBs) deployed at the center of C2 (AOFB 33) and C5 (AOFB 29) provided additional ocean observations (see https://www.oc.nps.edu/~stanton/fluxbuoy and Gallaher et al., 2016). Here we focus on the turbulent velocity observations obtained from the custom-built AOFB flux packages that included a 4-path acoustic travel-time current meter. The flux packages were initially located at ~4.5 m depth, ~2.5 m below the initial ice-ocean interface. The AOFBs measured the three-dimensional ocean velocity at 2 Hz for 35 minutes every 2 hours.

2.1.2 Wind and ice observations

Wind velocity was directly observed using an Autonomous Weather Station (AWS) at the center of each instrument cluster (C2—C5). Wind velocity relative to the ice velocity was measured 2 m above the ice every 15 minutes. For this analysis, the AWS wind direction estimates have been adjusted to account for apparent biases in instrument heading by aligning the AWS wind direction on timescales longer than 2 days with the direction of 10-m European Center for Medium-Range Weather Forecasts (ECMWF) Interim Reanalysis (ERA-Interim) winds (Dee et al., 2011) interpolated to the time-varying location of each buoy cluster. Wind speed and direction time series were constructed by interpolating to the times of the 250-m ITP-V profiles. Era-Interim wind speed was utilized at C2 after 27 August and at C5 after 22 September when the wind sensors stopped working.

Ice Mass Balance (IMB) buoys were deployed to measure air temperature and profiles of ice and near-surface ocean temperature from which ice elevation and ice draft were derived. Each cluster of instruments contained 5 IMB systems (Scottish Association for Marine Sciences (SAMS) IMBs; Jackson et al., 2013), with the central IMB co-located with the AWS, ITP-V and AOFB, and the other four forming a 5-km square around the cluster (**Figure 2c**). IMBs stopped telemetering and melted out of the ice in late August to early September when minimum measured ice drafts of 0.1–0.5 m depth were reported (**Figure 4b**).

2.2 IceBridge, drill-hole, and remote sensing observations

Operation IceBridge (Koenig et al., 2010) overflew C2 on 18 March 2014 just after its deployment (**Figures 3** and **5**). Seven repeat passes were flown, situated about 300 m from the central instruments (most passes were centered about a series of markers denoted as 'survey line' and visible in **Figure 5a**). Data from the Digital Mapping System (DMS, a high-resolution camera system mounted on the aircraft) and Airborne Topographic Mapper (ATM, a lidar) were used to estimate the elevation of the ice with a swath width of ~250 m (Krabill et al., 2002; Petty et al., 2016).

Directly beneath the IceBridge flight line at C2, a ground team obtained drill-hole data through the ice every 50 m along a 2-km segment during the ice camp operations (Beckers et al., 2015). The drill-holes were located about 300 m from the central instruments and passed through the same survey line of markers as the overhead flights (see **Figure 5a**). Ice thickness, ice freeboard, and snow depth are reported here. In addition, two airborne electromagnetic (AEM) surveys along the drill-hole line yielded total (ice-plus-snow) thickness estimates every 6 m (Haas et al., 2010).

Remote sensing observations provide estimates of ice concentration and ice type. Between May and September, 100 TerraSAR-X satellite images collected at C2–C4 were used to determine ice concentration and ice type for 30 × 30 km boxes about each drifting cluster (Hwang et al., 2017). Ice type refers to the fraction of first-year ice (FYI) versus multi-year ice (MYI) within the 30 × 30 km box, and was determined from images in March–June (e.g., **Figure 6**). RADARSAT-2 satellite images (e.g., **Figure 7**) were also utilized to estimate ice concentration in 30 × 30 km boxes (Ortiz, 2017). Values from July to September were used in this study. Ice concentration from AMSR2 was also considered within 30 × 30 km boxes (Spreen et al., 2008).

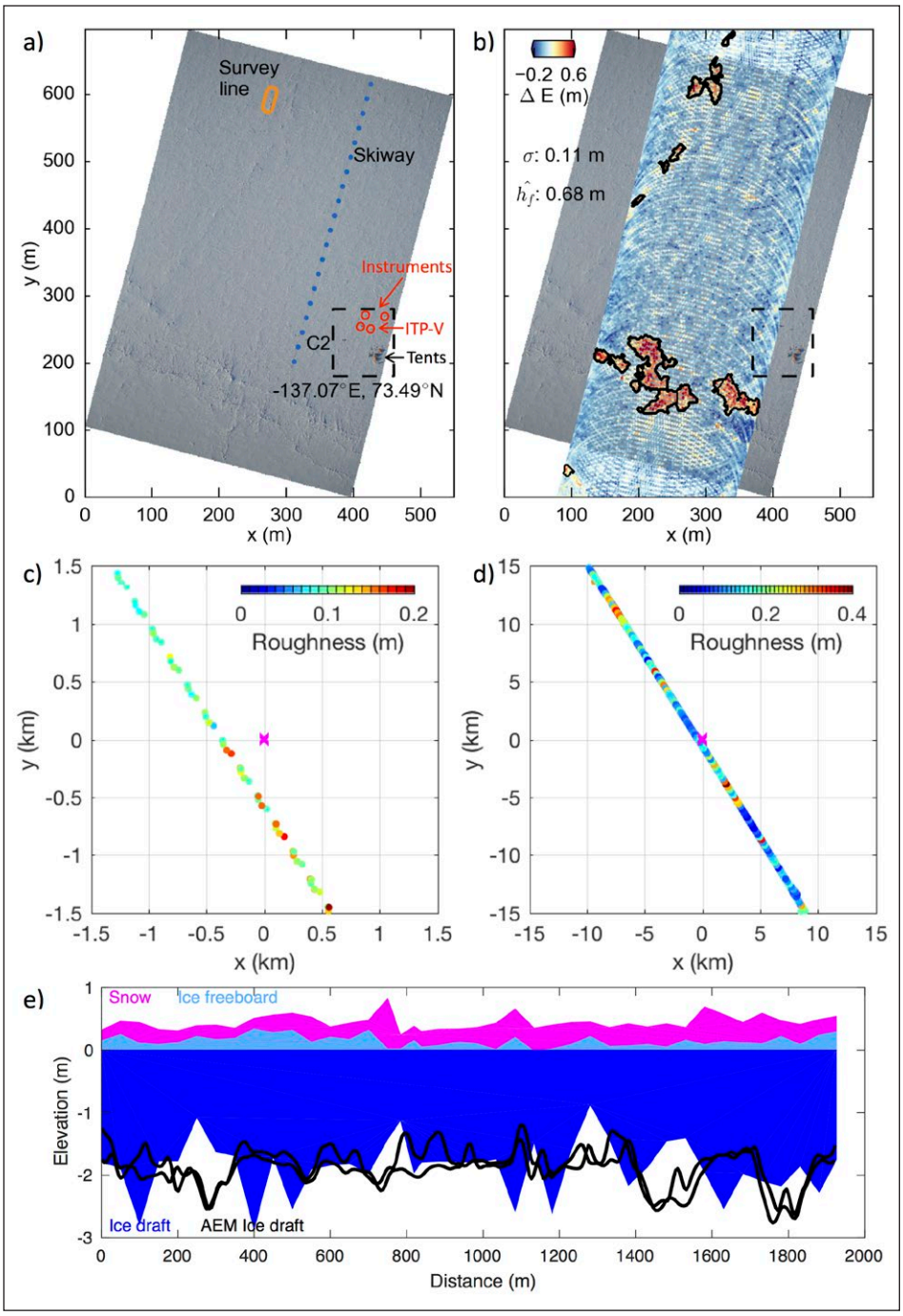

Figure 5: Ice topography at cluster 2 on 18 March 2014. IceBridge flight **a)** DMS-annotated to mark the ice-camp tents, central instrument cluster (red), skiway (dotted blue), and markers for the drill-hole survey line (orange), and **b)** ice elevation with the standard deviation of all ice elevations (sigma) and maximum feature height (h_f) indicated. Black contours denote the edges of individual ice features (see Petty et al., 2016). Average ice surface roughness in 0.2 km sections along the seven repeat IceBridge flight-paths in **c)** for a 3 × 3 km box and in **d)** for a 30 × 30 km box centered at C2 (magenta x). **e)** Profiles from drill-hole and AEM surveys. Drill-hole data (50-m point spacing) distinguish between snow depth (magenta), ice freeboard (light blue) and ice draft (dark blue). The AEM ice thickness data (observations at 6-m spacing) has been multiplied by 0.81 (the ratio of drill-hold draft to drill-hole thickness) to represent ice draft (black). DOI: https://doi.org/10.1525/elementa.241.f5

3. Methods

Daily averaged wind, ice, and ocean velocity are considered in this analysis (**Figures 8** and **9**). An hourly record of ice velocity was estimated from the first difference of the hourly GPS positions of the ITP-Vs. Absolute wind velocity was estimated by adding the measured relative wind velocity to the ice velocity. These wind and ice velocity records were then linearly interpolated to the times of ITP-V profiles and fixed depth records. Daily averaged speeds were computed from daily averaged velocity components, by averaging over all profiles (or fixed depth records) within ±12 hours of each profile (or fixed depth

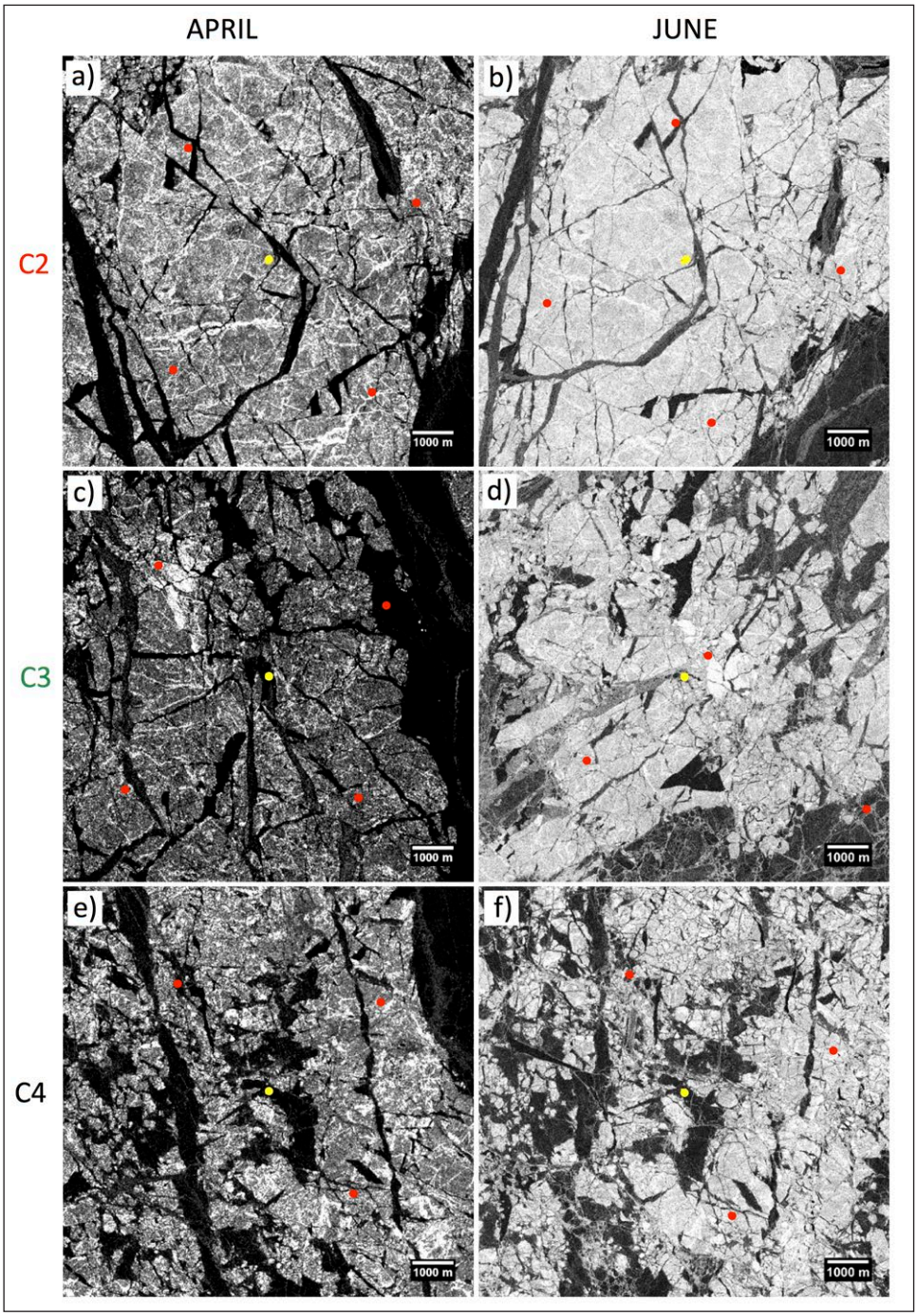

Figure 6: TerraSAR-X images in a 10 × 10 km box about the ITP-Vs. C2 in **a)** on 21 April and in **b)** on 5 June, C3 on **c)** 15 April and **d)** 5 June, and C4 on **e)** 21 April and **f)** 3 June. Within each image, lighter gray shades denote multi-year ice, darker gray shades denote first-year ice, and black denotes open water or new ice conditions. TerraSAR-X ice concentration for the early June images within 30 km of the ITP-Vs were 99–100% at all three clusters. Locations of the ITP-V (yellow square centered in each image) and IMBs (red symbols) are indicated. DOI: https://doi.org/10.1525/elementa.241.f6

record) so that near-inertial motions were effectively excluded. Wind, ice and ocean velocities were treated identically: only the wind and ice velocities at the corresponding profile (or fixed depth record) times were included in the daily averaged value. Daily averaged values are not used exclusively as some calculations rely on synoptic velocities (e.g., Ekman depth; see below).

Ice draft and thickness were utilized in estimates of ice-ocean drag coefficient and the analysis of the kinetic energy budget of the ice (see below). Ice draft, z_{ice}, and ice thickness, h_{ice}, at each ITP-V were taken from the IMB at the center of each cluster. Ice thickness is most directly estimated from each IMB. Ice draft is derived assuming ice and ocean densities of 917 kg m^{-3} and 1023 kg m^{-3}, which was sufficient for our purposes. There were no data from the central IMB at C5; ice draft was derived from the average melt/growth rate from the surrounding IMBs at C5 applied to the ice draft derived from the thickness of the

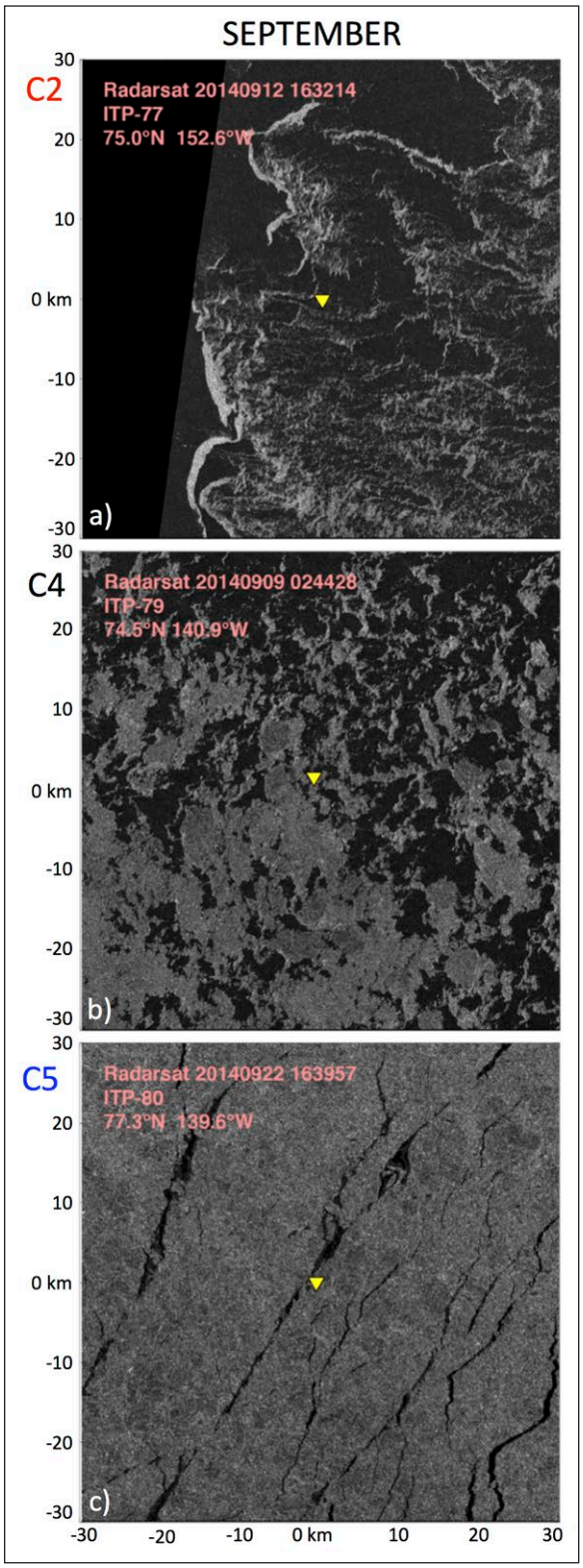

Figure 7: RADARSAT-2 images in a 60 × 60 km box about the ITP-Vs. a) C2 on 12 September, **b)** C4 on 9 September, and **c)** C5 on 22 September. These images correspond to estimated RADARSAT-2 ice concentrations of 42%, 58%, and 95%, respectively. Yellow triangles indicate the ITP-V position at the time of image acquisition. Within each image, open water is indicated by black pixels, while sea ice is indicated by gray pixels. RADARSAT-2 data and products copyright MacDonald, Dettwiler and associates LTD. 2014, all rights reserved. DOI: https://doi.org/10.1525/elementa.241.f7

hole through which the ITP-V was deployed. At C2, the IMB record ended prior to the ITP-V record (**Figure 3**).

Mixed layer depth was estimated for each profile using a density difference threshold of 0.25 kg m^{-3} from the shallowest observation. This criterion places the mixed layer base atop the zone of strong stratification at the base of the surface layer where strong velocity shear is frequently observed (**Figure 9**). Note that stratification above the shallowest ITP-V measurement depth of ~6.5 m is not accounted for.

An Ekman depth, D_E, was estimated for each individual velocity profile. Profiles of ocean speed were fit to an exponential function in depth:

$$\left\{\left[u(z)-u_{geo}\right]^2+\left[v(z)-v_{geo}\right]^2\right\}^{1/2}=V_0e^{-z/D_E} \qquad (1)$$

where V_0 and D_E are the fitted parameters and u_{geo} and v_{geo} are the meridional and zonal components of a reference velocity. Equation 1 is applicable to steady-state conditions with constant viscosity and neutral buoyancy (Ekman, 1905). The reference velocity was taken to be the velocity 2 m above the mixed layer depth; a deeper level was not used to avoid the strong velocity shear at the mixed layer base and the influence of halocline eddies (**Figure 9**). Using smaller density difference criteria to define the mixed layer depth did not result in significant changes in estimated Ekman depths. Throughout this analysis, Ekman depths larger than 70 m or negative values (that corresponded to ocean velocity increasing with depth) were excluded.

The thickness of the logarithmic boundary layer, h_{BL}, was estimated using the daily averaged Ekman depth as:

$$h_{BL}=0.05D_E \qquad (2)$$

(Shaw et al., 2008), which is appropriate for winter conditions with mixed layers tens of meters deep. With summer mixed layers and Ekman layers 10-m thick or shallower, the appropriate choice for h_{BL} is more uncertain, but the above represents a reasonable estimate. The depth of the bottom of the logarithmic boundary layer, equivalent to the top of the Ekman layer, is $z_{ice}+h_{BL}$.

The turbulent momentum flux, $\langle u'w'\rangle$ and $\langle v'w'\rangle$, was estimated from ITP-V and AOFB velocity observations. For the ITP-V data, each fixed depth velocity record was smoothed with a 4-second low-pass filter to remove higher-frequency noise, detrended, and then directly correlated (see also Cole et al., 2015). Only fixed depth records shallower than 10 m were considered, and some additional records were excluded from interpretation due to very shallow stratification (in July and August; see Section 4.2.3). For the AOFB, turbulent flux observations were estimated from spectral covariance of horizontal and vertical velocity over a specified frequency range as described in Gallaher et al. (2016). The resulting turbulent flux estimates represent an average over the respective instrument sampling period (20 minutes for the ITP-V and

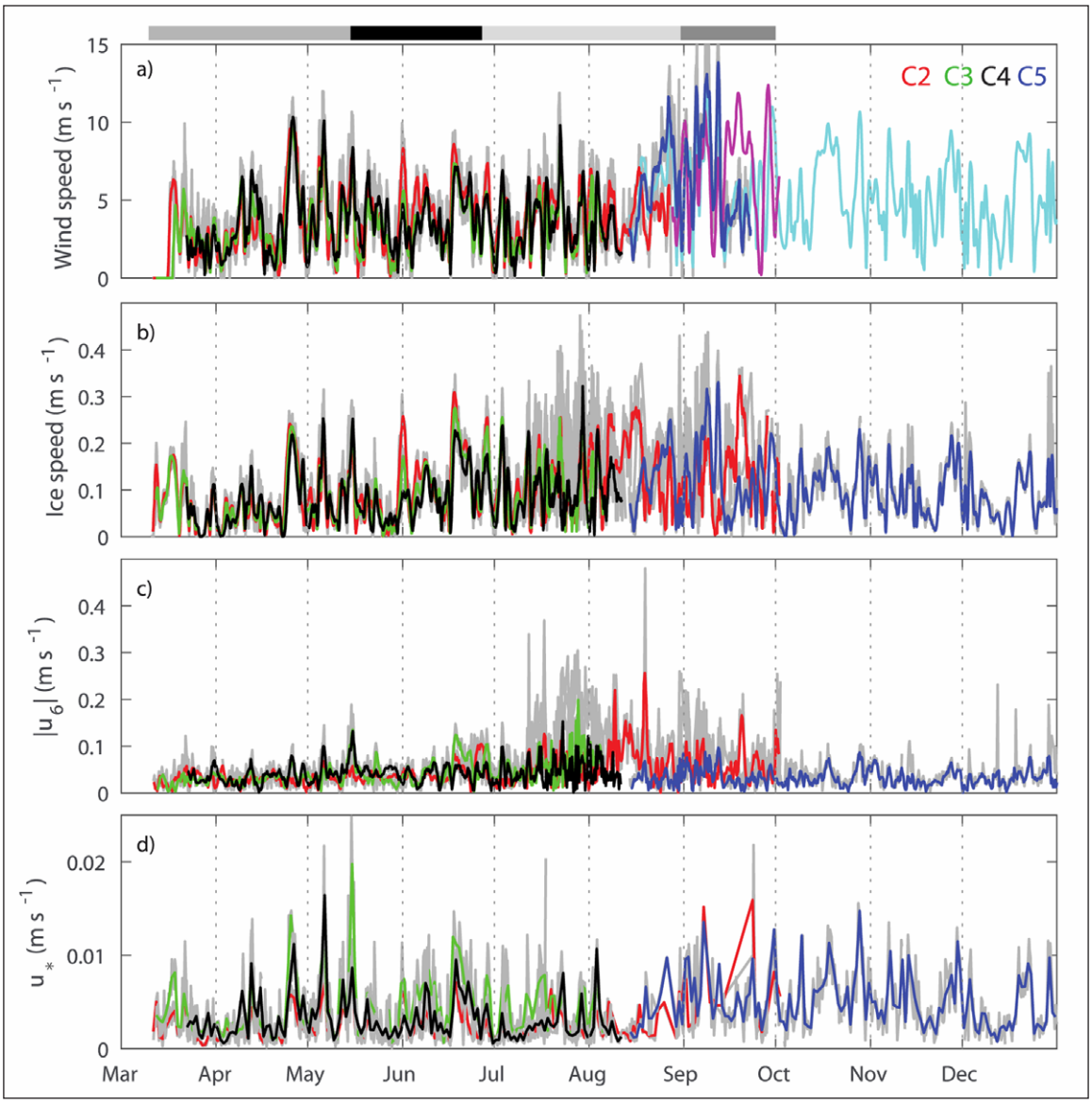

Figure 8: Time series of wind, ice, and ocean speeds. a) Wind speed, **b)** ice speed, **c)** 6-m ocean speed, and **d)** friction velocity at 6.5-m depth at C2–C5. Instantaneous values are in gray, with daily averaged values in color (velocity components are averaged prior to calculating speed). Daily averaged Era-interim wind speed is additionally shown at C2 after 27 August (magenta) and at C5 (light blue). Gray bars as in Figure 3. DOI: https://doi.org/10.1525/elementa.241.f8

35 minutes for the AOFB). In both cases, the friction velocity, u_*, was then estimated as:

$$u_* = \left(\langle u'w'\rangle^2 + \langle v'w'\rangle^2\right)^{1/4} \quad (3)$$

and referred to in the following as u_{*4} and u_{*6} for the AOFB observations at ~4.5 m depth and ITP-V observations at ~6.5 m depth, respectively. Differences between the two methods used to calculate $\langle u'w'\rangle$ and $\langle v'w'\rangle$ are minor (see also Section 4.2.1). Daily averaged u_{*4} and u_{*6}, which average all data within ±12 hours of each AOFB or fixed depth ITP-V record, were considered in this analysis.

ITP-V observations at 6.5-m depth were extrapolated to give values of the friction velocity, u_{*0}, and ocean current speed, u_0, at the top of the Ekman layer (at a depth of $z_{ice} + h_{BL}$). Cluster 2 ice draft was taken to be 0 m after the IMB record ended (from 27 August through September) for this calculation. Daily averaged Ekman depth was used to extrapolate u_6, the average velocity over each 20-minute fixed depth record, and u_{*6} to the depth of daily averaged $z_{ice} + h_{BL}$ via Equation 1; the friction velocity was assumed to have the same decay rate as ocean velocity. If the magnitude of the extrapolated u_0 was larger than that of the daily averaged ice velocity, the extrapolation was considered unrealistic and u_0 and u_{*0} were set equal to u_6 and u_{*6}, respectively. This situation occurred most frequently with shallow mixed layers in July. The direction of u_0 and u_{*0} were not extrapolated, and so these vectors are aligned with u_6 and u_{*6}.

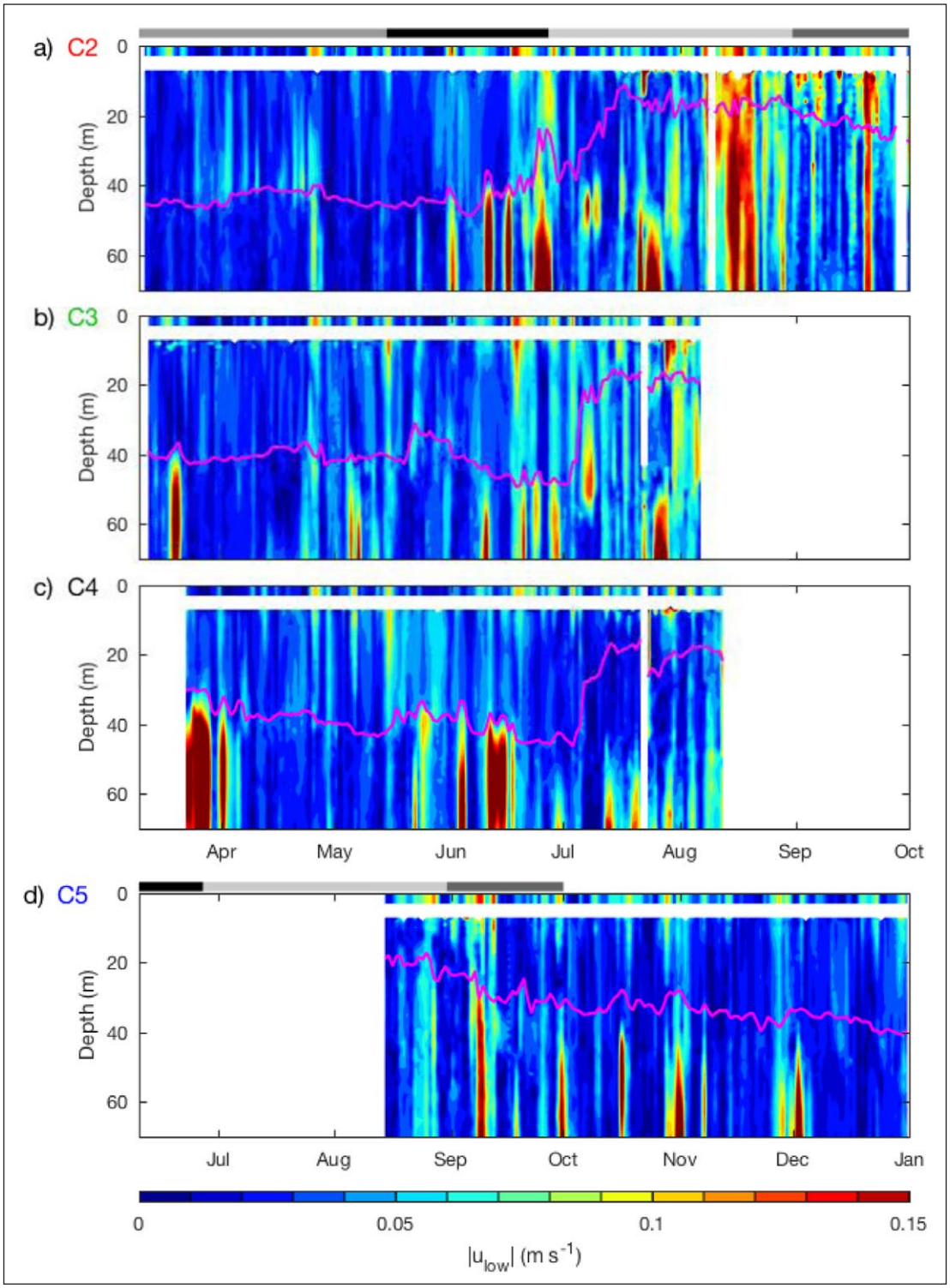

Figure 9: Daily averaged current speed in the upper 70 m. Shown by cluster: **a)** C2, **b)** C3, **c)** C4, and **d)** C5. Daily averaged ice speed scaled by 0.5 is shown in a band from depths of 0–3 m, and daily averaged mixed layer depth is shown in magenta. Velocity components are averaged prior to calculating speed. Note the different months for C5. Speeds in excess of 0.15 m s^{-1} correspond to the upper portions of halocline eddies (e.g., Zhao et al., 2014). Gray bars as in Figure 3. DOI: https://doi.org/10.1525/elementa.241.f9

Given observations throughout the logarithmic boundary layer and Ekman layer, ice-ocean stress, τ, was parameterized as:

$$\tau = u_*^{\,2} = C_d \left|u_{ice} - u_{ref}\right| \left(u_{ice} - u_{ref}\right) \exp\left(i\beta\right) \qquad (4)$$

where C_d is the ice-ocean drag coefficient, β is the turning angle, and u_{ref} is a reference velocity (McPhee, 2008). The ice-ocean drag coefficient is given by:

$$u_*^{\,2} = C_d \left(u_{ice} - u_{ref}\right)^2 \qquad (5)$$

and the turning angle is defined following, e.g., **Figure 4** of McPhee (2012) as that between the ice velocity and the vector connecting the ice velocity to u_0 (**Figure 1b**). The reference velocity can be the undisturbed ocean velocity (e.g., that just below the Ekman layer), or a level closer to the ice (Lu et al., 2011). Large ice-ocean drag coefficients correspond to decreased shear between the ice and ocean for the same friction velocity. Turning angles depend on the direction as well as the magnitudes of the ice and ocean velocities (**Figure 1b**); for an ocean velocity that is 50% of the ice velocity, turning angles would be 5° and 28° for a 5° and 85° offset between u_{ice} and u_0, respectively. Larger turning angles correspond to larger rotations between u_{ice} and u_0 or to a larger magnitude of u_0 relative to u_{ice}.

Two estimates of the ice-ocean drag coefficient were made using Equation 5 by employing different friction velocities and reference velocities. Specifically:

$$u_{*0}^2 = C_{d0}\left(u_{ice} - u_{geo}\right)^2 \tag{6a}$$

$$u_{*6}^2 = C_{d6}\left(u_{ice} - u_6\right)^2 \tag{6b}$$

where ice speed, reference velocity (u_{geo} or u_6), and friction velocity (u_{*0} or u_{*6}) were used for each fixed depth record, and computed using daily averaged ice and ocean velocity components. The corresponding turning angles, β_0 and β_6, similarly used u_{geo} as in Equation 6a and u_6 as in Equation 6b as the reference velocity (and were the angles between the daily averaged $u_{ice} - u_{ref}$ and the vector connecting daily averaged $u_{ice} - u_{ref}$ to daily averaged $u_0 - u_{ref}$ in both cases; daily averaged velocity components were used). The geostrophic velocity, u_{geo}, was taken to be the measured ocean velocity 2 m above the base of the daily averaged mixed layer (the same reference velocity used to estimate Ekman depth). Note that u_0, and thus both estimates of turning angle, as well as C_{d0} are dependent on ice draft and estimates of logarithmic boundary layer thickness. These two estimates of C_d and turning angle were formally made for the entire time series; disagreements between the two estimates (along with hydrographic and melt pond drainage data) illustrate when ice-ocean drag coefficients cannot be reasonably determined from these observations (see Section 4.2.3).

The roughness length scale, z_0, was estimated from u_{*0} at the top of the Ekman layer. Within the logarithmic boundary layer, the relationship between $u_{ice} - u_{geo}$ and u_{*0} defines a roughness length scale:

$$\kappa\left(u_{ice} - u_{geo}\right)/u_{*0} = \log\left(z_m / z_0\right) \tag{7}$$

where κ = 0.4 is von Kármán's constant, and z_m is the distance from the measurement depth to the bottom of the ice (McPhee, 2002, 2008). Using extrapolated u_{*0} at the bottom of the logarithmic boundary layer, z_m is the thickness of this layer (h_{BL}). As C_{d0} encompasses the relevant velocities, the daily averaged roughness length was estimated as:

$$z_0 = h_{BL} / \exp(\kappa C_{d0}^{1/2}) \tag{8}$$

using daily averaged h_{BL} and C_{d0}. Only records for which $u_{*0} > 3 \times 10^{-3}$ m s^{-1} were included.

Analysis of terms in the kinetic energy budget for the ice floes supporting the instrument clusters were constructed following Leppäranta (2011, see Equation 5.16). The per unit area energy associated with the wind work and ocean work on the ice, acceleration of the ice, and potential energy change due to motion across a sloped sea surface were estimated as:

$$Wind\ work = \rho_a C_{da}\left|u_a - u_{ice}\right|\left(u_a - u_{ice}\right)\cdot u_{ice} / h_{ice}\rho_{ice} \tag{9a}$$

$$Ocean\ work = \rho_0 C_{d6}\left|u_{ice} - u_6\right|\left(u_{ice} - u_6\right)\cdot u_{ice} / h_{ice}\rho_{ice} \tag{9b}$$

$$acceleration = \frac{d}{dt}\left[u_{ice}^2 + v_{ice}^2\right] \tag{9c}$$

$$sea\ surface\ motion = -g\left[u_{ice}\frac{\partial\eta}{\partial x} + v_{ice}\frac{\partial\eta}{\partial y}\right] \tag{9d}$$

where C_{da} is an air-ice drag coefficient; ρ_a, ρ_{ice}, and ρ_0 are the density of air, ice, and ocean, taken to be 1.0, 917, and 1023 kg m^{-3}, respectively; and η is the sea surface height. Sea surface height was estimated using daily-averaged ocean velocity vertically averaged over 20–40 m depth (beneath the Ekman layer) and assuming a geostrophic balance. The specific atmospheric and oceanic drag coefficients used in Equations 9a and b, which are allowed to vary with time and between clusters, are detailed in Section 4.3. The residual of these four terms theoretically corresponds to the effects of the internal ice stress. These terms were only considered prior to 26 August when the IMB at C2 stopped telemetering data.

4. Results

4.1 Overview of the air-ice-ocean conditions

Ice concentration was similar at C2–C4 through mid-July (**Figure 4a**). At C2–C4, AMSR2 ice concentration first fell below 98% coverage on 25 April, and subsequently fell to 80% ice concentration (or below) on 22 June. Ice concentrations derived from TerraSAR-X imagery were similar to those from AMSR2 through July, but were slightly larger during August–September. Ice concentration derived from RADARSAT-2 images had the highest values of these remote sensing products, and showed that ice remained in the immediate vicinity of C2 and C4 over the entire time series (including in September; e.g., **Figure 7**). By September (late summer), the ice seen by RADARSAT-2 consisted of streaks and patches of small individual ice floes at C2, somewhat larger streaks and patches of ice floes at C4, and a nearly full ice cover at C5 (**Figure 7**; see also Arntsen et al., 2015 and Hwang et al., 2017). During August and September, all three ice concentration estimates showed more open water at C2 than at C4. At C5, AMSR2 ice concentration ranged from 80–100%

through late September, and then remained above 95% through December, consistent with RADARSAT-2 images (**Figures 4a** and **7c**).

Wind speeds at the clusters were highly correlated with similar, modest magnitudes at C2–C5 throughout 2014 (**Figure 8a**). Daily averaged wind speed exceeded 10 m s^{-1} on only a few occasions at C2–C4 including 26 April, 22 July, and around 1 September. High-frequency fluctuations from the daily averaged wind speeds were small in magnitude throughout the record (**Figure 8a**) with no spectral peak at the near-inertial frequency (not shown). Note that C5 was deployed just prior to a period of steadily increasing winds from 13–27 August and sampled a period of elevated winds from 5–12 September, which were also observed at C2.

Ice and ocean speeds were variable throughout the study period. Daily averaged ice speed was well correlated with daily averaged wind speed (**Figure 8a** and **b**; $r^2 > 0.75$), suggesting the ice was in free drift to first order from March through December. In contrast to wind speed, high-frequency ice speed fluctuations from the daily averages were significant in July – October due to near-inertial motions. Daily averaged ocean speed at 6 m depth (**Figure 8c**) was typically less than 0.1 m s^{-1}, and effectively uncorrelated with ice speed over the entire record ($r^2 < 0.2$). The largest ocean speeds were associated with high wind and/or ice velocity events, with a tendency for larger speeds in August and September. As with ice speed, deviations from the daily averaged ocean speed were large in July – October due to near-inertial currents. Friction velocity was correlated with ice velocity ($r^2 > 0.6$), and so correlated between the clusters with large values associated with high wind and ice velocities (**Figure 8d**). Further details of the wind, ice, ocean, and friction velocities are reported in the remainder of this section.

The surface layer stratification and currents showed typical conditions for the Canada Basin in recent years. The mixed layer was 40 m deep from March through late June, and then shoaled over an approximately one-week period to 10–15 m depth (**Figure 9**; see also Gallaher et al., 2016). The shallow summer mixed layer persisted from mid-July through August, and then gradually deepened in September. The thermodynamic evolution of the IOBL at these clusters, observed by the IMBs, AOFBs, and ITP-Vs, is discussed in Gallaher et al. (2016). Of relevance here is that maximum melt pond coverage at C2 occurred on 27 June, with draining of those melt ponds over the next 9 days, and an observed freshwater signal at 4 m depth in the ocean on 11 July. Shallow, 1–2 m thick ephemeral mixed layers caused by melt water input were inferred from 27 June to 31 July (these resided between the ice-ocean interface and the shallowest measurement depth). The timing of melt pond drainage was similar at C3 and C4, with drainage occurring prior to an observed freshwater signal at 4–6 m depth. Ocean currents at 6 m depth were representative of the mixed layer below, with ocean speeds that most often decayed with depth (**Figure 9**). Below the mixed layer base, ocean currents were strongest in eddies and during times of open water.

4.2 Seasonal cycle of momentum transfer

Ice topography will be used to refer collectively to the physical features of the ice that affect the coupling of the air-ice-ocean system. Such physical features and phenomena include ice ridges, the break up of floes with time, and their manifestation as air-ice drag coefficients, ice-ocean drag coefficients and ice roughness lengths.

In this subsection, we address ice-ocean drag coefficients and other indicators of momentum transfer in a sequence of time periods: March – 15 May, 16 May – 27 June, 28 June – 31 August, 1 September – 1 October, and 1 October – 31 December (**Figure 4**). The boundaries of these time periods are defined based on specific events: changes to the ice-ocean drag coefficient were observed to begin near 15 May, melt ponds began to drain at C2 on 27 June, the mixed layer became sufficiently deep on 31 August, and the ITP-V at C2 was recovered on 1 October (**Figure 3**). These time periods are introduced here for clarity; the specific events are addressed below in more detail. Note that these time periods were not chosen with respect to ice concentration, but period boundaries do roughly coincide with changes to ice concentration (**Figure 4**).

4.2.1 March – 15 May

Above-ice observations in March at C2 indicated a preponderance of smooth ice in the region (**Figure 5**). Cluster 2 (and the nearby survey line) was deployed on a large ice floe consisting of level ice with limited hummocks and ridges, and was so smooth that the Twin Otter could land on the ice floe (as opposed to refrozen leads at C3 and C4; Beckers et al., 2015). The IceBridge DMS and ATM data show variations in ice elevations of typically less than 0.1 m with a few isolated features with maximum elevations of 0.6 m (that were located more than 100 m away from the instruments; **Figure 5a** and **b**). IceBridge data over 2009–2014 within the Canada Basin had mean feature heights near 1 m (Petty et al., 2016), suggesting that the region within ~1 km of C2 was smoother than typical ice in the Canada Basin. Ice roughness computed every 40 m along the fight path (see https://nsidc.org/data/docs/daac/icebridge/evaluation_products/sea-ice-freeboard-snowdepth-thickness-quicklook-index.html) and averaged into 200-m bins shows ice roughness less than 0.2 m for the region within 1.5 km of the instrument cluster (**Figure 5c**), as well as the region within 5–10 km (**Figure 5d**). The lowest ice roughness estimates of 0.1 m or smaller are likely indicative of interspersed refrozen leads in the vicinity of C2, consistent with **Figure 6a**.

Drill-hole and AEM data near C2 also show this smooth ice surface and corresponding under-ice topography (**Figure 5e**). The mean ± standard deviation of the freeboard and ice draft from drill-hole measurements at C2 was 0.14 ± 0.09 m and 1.9 ± 0.4 m, respectively. Mean ice-drafts of 1–2 m have been typical of the Canada Basin in winter in recent years (Krishfield et al., 2014). The total thickness of the more finely spaced AEM data along the 2-km drill-hole survey line had a mean ± standard deviation of 2.4 ± 0.4 m, comparable to the drill-hole total thickness, and did not show the presence of any significant keels.

Ice draft observations from the drifting IMBs indicate ice conditions over a 5-km scale at each cluster (e.g., **Figure 2c**). Of the 15 IMBs deployed at C2–C4, 13 had initial ice drafts of 1.2 to 1.6 m (**Figure 4b**). The other two IMBs had initial ice drafts of 2.7 and 3.2 m, and were located at C3 initially to the west of the ITPV and AOFB (**Figure 2c**). This thicker ice persisted through the melt period and remained about 2 m thicker than the floes at the other IMB sites through to early September (**Figure 4b**). At C5, the two IMBs reported ice drafts of 1.6–2.0 m, with the ITP-V initially deployed through a hole in the ice floe corresponding to a 2.3-m ice draft.

The fraction of multi-year ice was similar at C2–C4 but distributed differently. The 30 × 30 km boxes centered about each cluster consisted of a conglomerate of MYI floes embedded within FYI (Hwang et al., 2017); **Figure 6** shows 10 × 10 km boxes (that are representative of the larger areas) in which individual features are more evident. The ITP-V at C2 was deployed on multi-year ice, while C3 and C4 systems were deployed on FYI adjacent to MYI (**Figure 6**). With slight variation depending on the specific TerraSAR-X image analyzed, the 30 × 30 km box centered at C2 consisted of 56–61% MYI, and those for C3 and C4 indicated 60–66% and 62–67% MYI, respectively (Hwang et al., 2017). The typical size of the multi-year ice floes varied between clusters, with C2 having larger floes of MYI compared with C3 and C4 (**Figure 6**; see also Hwang et al., 2017). Cluster 5 was deployed in a ridged area with an initial ice thickness of 2.3 m between two ~1 m thick floes, indicating that multiyear ice was present in the area.

Under-ice roughness was first investigated from ice-ocean drag coefficient estimates that derive from turbulence observations near the top of the Ekman layer. Ekman depths were generally shallower than the mixed layer depth and ranged from 15–30 m (**Figure 10**), which corresponds to a log-layer that is 0.7–1.5 m thick (see Equation 2). A 2-m ice draft together with a 1.5-m log-layer corresponds to an estimated top of the Ekman layer at 3.5-m depth, shallower than the turbulent flux measurements. At C2, the close agreement between u_{*4} and u_{*6} (**Figure 11**) further supports the assertion of a shallow log-layer and observations within the Ekman layer.

Ice-ocean drag coefficients varied significantly between clusters (**Figure 12**). Weekly median C_{d6}, C_{d0}, β_6 and β_0 were less variable then their day-to-day estimates, and show the spatial and temporal variations of interest (e.g., **Figure 12a**). Estimates of C_{d6} at C2 (median $C_{d6} = 1.0 \times 10^{-3}$) were consistently lower by a factor of three than that at C3 and C4 (median $C_{d6} = 2.8 \times 10^{-3}$ and 3.6×10^{-3}, respectively; **Figure 12a**) over March – 15 May. Weekly median C_{d0} was somewhat larger than C_{d6} (**Figure 12b**), with differences between the two estimates smaller than the differences between clusters. As confirmed by analysis of the later time periods, this factor of three difference between the clusters results directly from the larger MYI floe sizes at C2. Turning angles were variable between the clusters as well with median β_6 of 4°, 8° and 11° at C2, C3, and C4, respectively, smaller than median β_0 of 24°, 20°, and 27°. The smaller values at C2 are consistent with its smaller ice-ocean drag coefficient (McPhee et al., 2012). May 15 was chosen as the boundary between the first and second time periods since there was no clear trend in weekly median values of C_{d6} and C_{d0} prior to 15 May (in contrast to the following time period), and 15 May was when the C3 and C4 drag coefficient estimates became distinct. It could be argued that this dividing point does not occur until June 1st, but no later.

Another indicator of momentum transfer is the depth to which ocean currents were accelerated by the ice and winds, which is affected by ice roughness/topography. Currents within the mixed layer (during March – 15 May) were small in magnitude apart from a few events with elevated wind and ice speeds (**Figure 9**). For the wind events in April and early May, elevated ocean currents extended throughout the upper 30–40 m at C4, to somewhat shallower depths at C3, and were weakest and shallowest at C2, consistent with estimated ice-ocean drag coefficients.

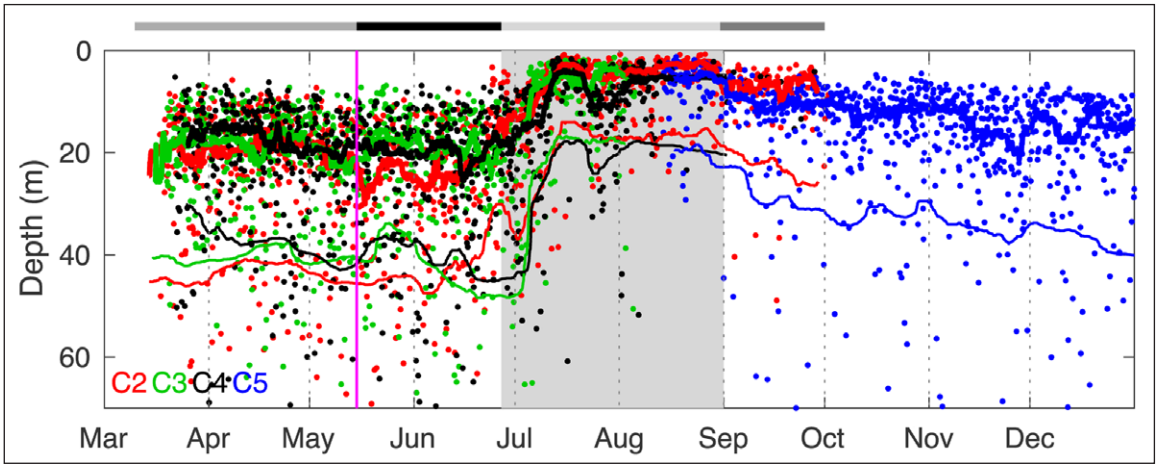

Figure 10: Time series of Ekman depth and mixed layer depth. Instantaneous Ekman depths at C2–C5 (dots), the 7-day median Ekman depth (thick), and the 7-day median mixed layer depth (thin) are shown. Gray bars as in Figure 3. Magenta line as in Figure 4. The third time-period is shaded gray to denote when very shallow stratification may not have been observed. DOI: https://doi.org/10.1525/elementa.241.f10

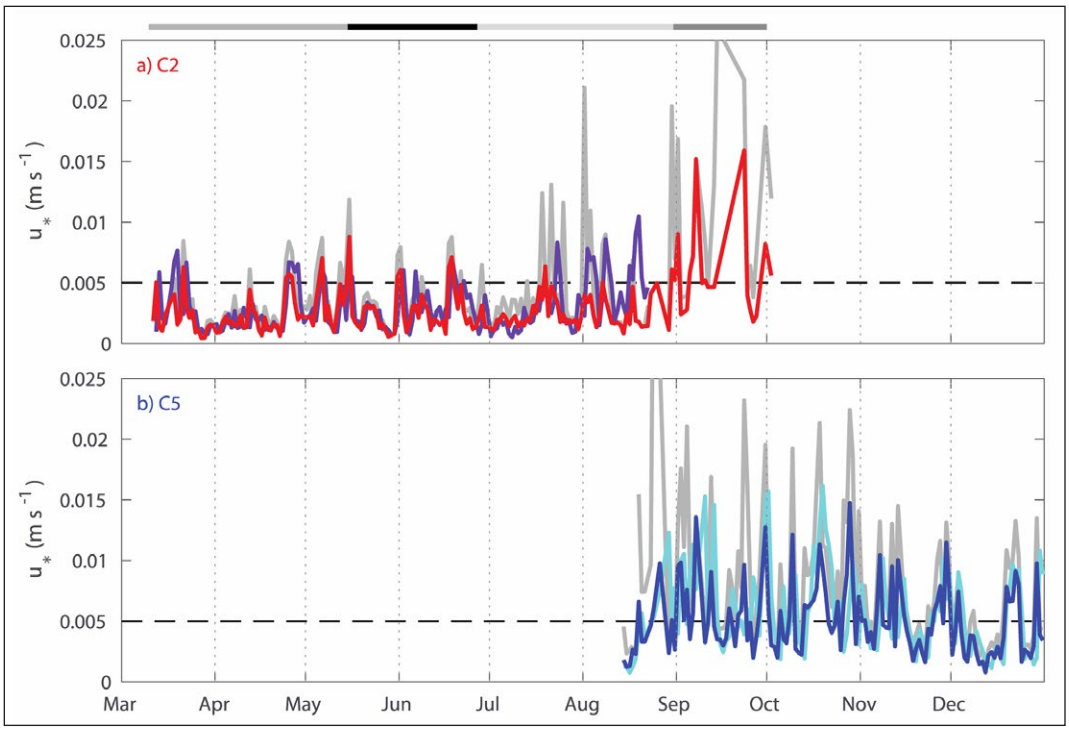

Figure 11: Daily averaged friction velocity from ITP-V and AOFB data. a) C2 with u_{*6} (red) and u_{*4} (purple), and **b)** C5 with u_{*6} (blue) and u_{*4} (light blue). Extrapolated u_{*0} estimates (gray) are based on daily averaged Ekman depths (and utilizing u_{*6}). Gray bars as in Figure 3. DOI: https://doi.org/10.1525/elementa.241.f11

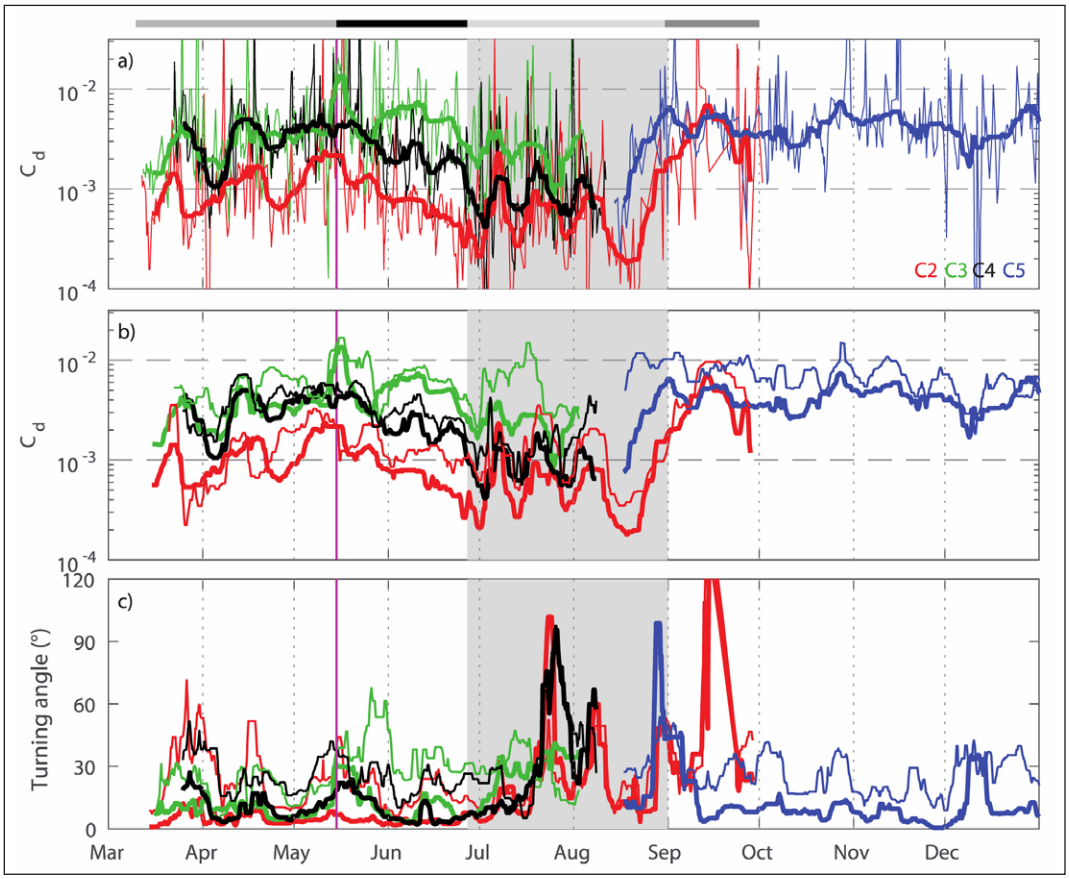

Figure 12: Time series at C2–C5 of ice-ocean drag coefficient and turning angle estimates. a) C_{d6} (thin) and its weekly median (thick), **b)** weekly median values of C_{d6} (thick, as in a) and C_{d0} (thin), and **c)** weekly median turning angle estimates β_6 (thick) and β_0 (thin). Daily averaged friction velocity and velocity components are used. Gray bars, magenta line, and shading as in Figure 10. DOI: https://doi.org/10.1525/elementa.241.f12

4.2.2 16 May – 27 June

At C3, the ice cover rearranged significantly and the ice-ocean drag coefficient increased. Individual MYI floes and other distinct features of the ice cover in mid-April were no longer recognizable by 5 June (**Figure 6c** and **d**). The GPS positions of the IMBs and ITP-V show that this rearrangement began during a wind event on 26 April. The IMB initially located to the northwest of C3, that reported the 2.7-m ice draft, translated to within 3 km of the ITP-V by 30 April, 2 km by 17 May (the start of this time period), and 1 km by 4 June (**Figure 6c** and **d**). The movement of this thick ice closer to the ITP-V resulted in a near doubling of C_{d6} to a median value of 5.1×10^{-3} over 16 May – 27 June (compared with 2.8×10^{-3} over March – 15 May; **Figure 12b**). Turning angles also increased to 10° for β_6 and 35° for β_0 (**Figure 12c**), consistent with the increased ice-ocean drag coefficient (McPhee, 2012).

In contrast to C3, TerraSAR-X images from mid-April and early June at C2 and C4 (**Figure 6a, b, e, f**) show that the ice within ~5 km of each ITP-V was intact and largely unchanged during this time period. Individual MYI floes and other distinct features are recognizable in each pair of images. Minor rearrangement of features more than 5 km from the ITP-V was evident at C4 (but not at C2). Median values of C_{d6} (and C_{d0}) decreased by 20–30% at C2 and C4 to $C_{d6} = 0.8 \times 10^{-3}$ at C2 and 2.4×10^{-3} at C4, while maintaining the factor of three difference observed during March – 15 May. Turning angles also decreased (compared with March – 15 May) with median β_6 values of 4° (C2), and 9° (C4), and median β_0 values of 18° (C2), and 22° (C4), again consistent with the decrease in C_d at C2 and C4 (McPhee et al., 2012).

4.2.3 28 June – 31 August

One of the distinguishing features during this time period was the presence of shallow stratification, which began as thin ephemeral mixed layers (inferred; see also Gallaher et al., 2016) that subsequently evolved into a 10-m thick traditional summer mixed layer (**Figure 9**). At C2, the agreement between u_{*6} and u_{*4} during July (**Figure 11**) resulted from the melt water layer (due to melt pond drainage that began on 27 June) remaining above the 4.5-m measurement depth. After July 15, the 6-m ocean currents were decoupled from the boundary layer with extrapolated u_{*0} occasionally much larger than u_{*4} or u_{*6}, indicative of shallow stratification (u_{*0} was also frequently set equivalent to u_{*6} at these times when extrapolated u_0 was larger than u_{ice} based on the observed Ekman depth). C5 had fewer instances of $u_0 > u_{ice}$ due either to the larger ice drafts at C5 or the higher ice concentration in August. At C2 and C5, u_{*4} was significantly larger than u_{*6} on occasion, indicative of shallow stratification between these measurement depths. For a very shallow mixed layer and constricted Ekman layer, it is possible that the measurements at depths of 4.5 and 6.5 m were near the bottom or even beneath the mixed layer and/or Ekman layer. Based on these momentum flux observations and the timing of melt pond drainage, our ice-ocean drag coefficient and ice roughness length estimates for the period between 28 June and 31 August are likely to have large errors and should be regarded with skepticism.

In July and August, the C_{d0} and C_{d6} estimates as well as β_0 and β_6 estimates were variable in time and less consistent with each other (**Figure 12b, c**). Estimates of C_{d0} and C_{d6} frequently disagreed by more than 50%, such as at C3 in early July and C5 in late August. The differences at C5 occurred even though ice concentration was above 80%, suggesting that the shallow summer mixed layer rather than the specific ice concentration (or ice floe size) was responsible for these discrepancies. Turning angles were larger during these summer months with large turning angles near August 1st. These discrepancies further indicate that the directly observed turbulent fluxes during these summer months are not representative of the stress at the ice-ocean interface, and it is not appropriate to draw conclusions based on the ice-ocean drag coefficients at these times.

Indirect indicators of momentum transfer, specifically the ratio of wind to ice speed (the Nansen number) as well as ice to ocean speed, show seasonal changes in the air-ice-ocean system. These are common indicators of momentum transfer within the air-ice-ocean system in the absence of turbulent or boundary layer observations. The ratio of daily-averaged 1) ice to wind speed, and 2) ocean to ice speed were considered for 28 June – 31 August, and compared to ratios over March – 15 May and 16 May – 27 June (**Figure 13**).

The ratio of wind to ice speed was most dependent on ice concentration (**Figure 13a, c,** and **e**). During any of the time periods considered, the Nansen number did not vary significantly with wind speed or between clusters C2–C4. The specific ratio varied by time period with values indistinguishable from 0.02 (50:1) during March – 15 May (consistent with past observations in primarily multiyear ice and full ice cover; McPhee, 2002), between 0.02 and 0.03 (30:1) during 16 May – 27 June, and between 0.03 and 0.04 during 28 June – 31 August. The August observations at C5 confirm that ice concentration was the primary factor influencing the Nansen number, with values consistent with 0.02 (50:1) at C5 in contrast to values at C2–C4 in lower ice concentrations. Larger wind to ice speed ratios were only observed as the ice concentration decreased, with ice roughness and ice speed having little effect, indicating that momentum was more easily transferred to the ice in partial ice cover.

The ocean speed to ice speed ratio varied primarily with ice speed, and also with ice roughness and concentration (**Figure 13b, d,** and **f**). For all time periods and all clusters, the ratio of ocean speed (averaged over 6–8 m depth) to u_{ice} decreased as the ice speed increased. Ocean speeds were similar to or larger than ice speeds for speeds less than 0.05 m s^{-1}, and up to a factor of 10 times smaller than ice speed for higher ice speeds, largely reflecting that ocean velocities were small regardless of the ice speed. Ratios were distinct between the clusters, especially for C2 with 25–75th percentiles that often did not overlap with C3 or C4, once ice speeds were larger than 0.1 m s^{-1} during March – 27 June and 0.05 m s^{-1} during July – August. The smallest ocean speeds were at C2, consistent with the

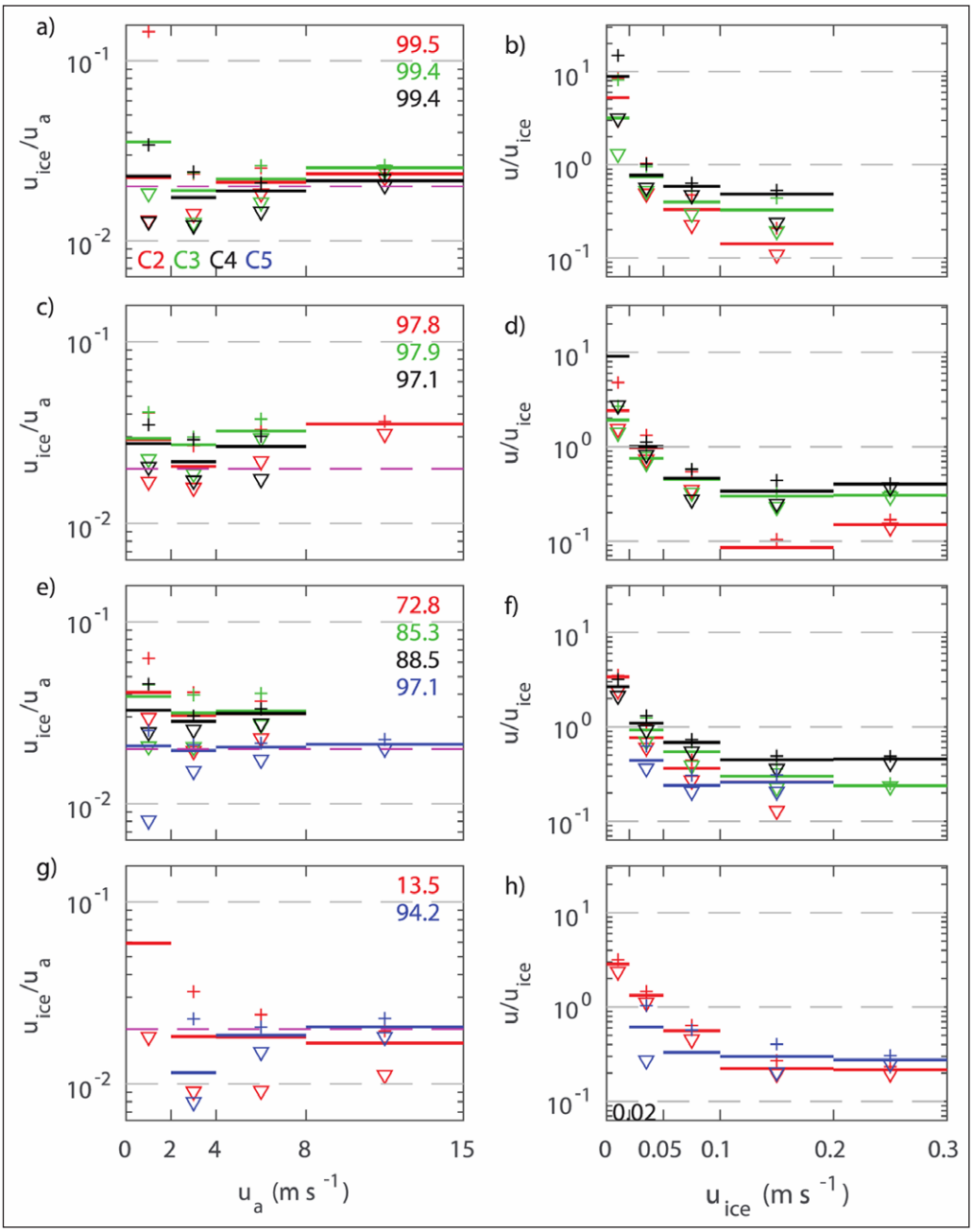

Figure 13: Wind, ice, and ocean speed ratios. Median (lines) and 25th (triangles) and 75th (plus symbols) percentiles in **a)** and **b)** over the period March – 15 May, in **c)** and **d)** over 16 May – 27 June, in **e)** and **f)** over 28 June – 31 August, and in **g)** and **h)** over 1 Sept – 1 October of in a) c) e) and g) ice speed to wind speed ratio as a function of wind speed, and in b) d) f) and h) ocean speed (averaged over 6–8 m depth) to ice speed ratio as a function of ice speed. Daily averaged velocity components were used in calculating ratios. Magenta dashed line in a) c) e) and g) corresponds to a ratio of 1:50 (0.02), and numbers (upper right) indicate the mean ice concentration (AMSR2) for each cluster and time period. DOI: https://doi.org/10.1525/elementa.241.f13

smooth ice and smaller ice-ocean drag observed at C2. In July and August, ratios were smallest at C5 (**Figure 13f**) despite the thick MYI near this cluster (**Figures 4b** and **7**), suggesting that momentum was more easily transferred to the ocean in low ice concentration conditions.

The depth to which ocean currents were accelerated by the ice and winds (**Figure 9**) shows the influence of shallow stratification on mixed layer currents. After the summer mixed layer shoaled, daily averaged upper ocean currents were larger, and more likely to extend throughout the full depth of the summer mixed layer (to 10–20 m depth) compared to March – 27 June.

Differences in momentum transfer were also evident from the average Ekman spiral in each time period (**Figure 14**). For this analysis, those profiles with ice velocity larger than 0.07 m s^{-1} (the median value over all clusters) were identified, the coordinate system for each wind, ice, and ocean profile was rotated so that the ice

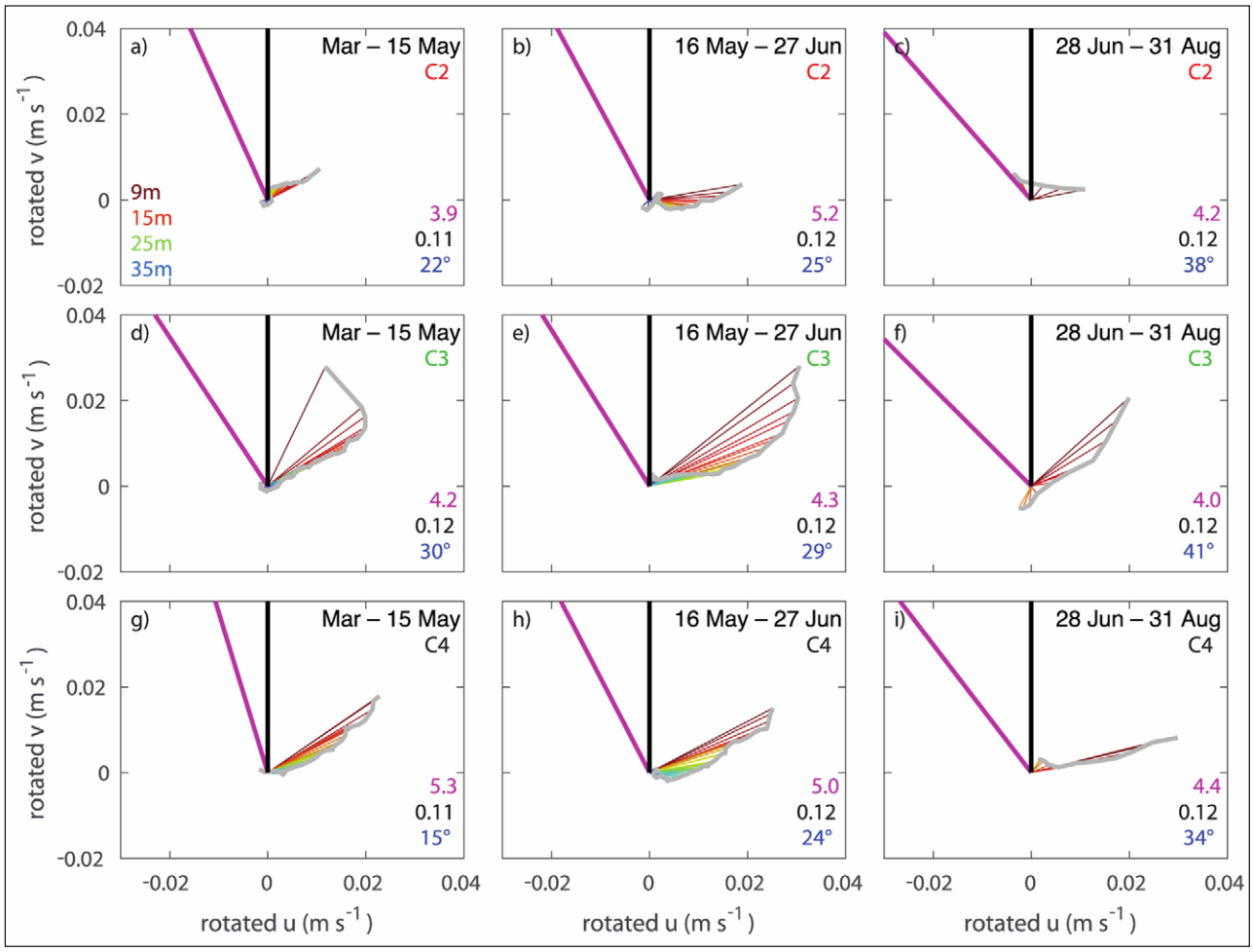

Figure 14: Ekman currents. Averaged wind (magenta), ice (black), and ocean (color) velocities relative to u_{geo} in **a)–c)** at C2, in **d)–f)** at C3, and **g)–i)** at C4 over the period, in a), d) and g) of March – 15 May, in b), e) and h) of 16 May – 27 June, and in c), f) and i) of 28 June – 31 August. Wind and ocean velocities were rotated so that the ice velocity was oriented northwards before averaging. Only data corresponding to a daily averaged ice velocity in excess of 0.07 m s^{-1} are included with ocean currents plotted from 9-m depth to the depth of the median reference depth (2 m above the mixed layer base). Daily averaged winds, ice, and ocean speed were used. The averaged wind speed (magenta in m s^{-1}), ice speed (black in m s^{-1}), and angle between wind and ice velocity (blue) are shown in the lower right. DOI: https://doi.org/10.1525/elementa.241.f14

velocity was oriented northwards, and all the selected profiles in a time period were averaged. Smaller ice speeds corresponded to very small ocean velocities (not shown). Overall, upper-ocean currents (relative to the velocity 2 m above the mixed layer base) had average speeds less than 0.04 m s^{-1}. The primary factor influencing the Ekman currents was the ice topography: the smallest currents that decayed most quickly with depth were observed at C2, which had the smoothest ice cover, and the clearest, most classic Ekman spiral was seen at C3, which had rougher ice. The influence of shallow stratification was evident during July – August: 9-m ocean currents at each cluster were comparable to those observed in March – June, but below 9-m depth, ocean currents decayed quickly with depth due to the shallow summer mixed layer. The largest differences between the ice and wind directions also occurred during July – August (34–41° versus 15–30° during March – 27 June).

4.2.4 1 September – 1 October

After 1 September, shallow stratification had been erased, again allowing estimation of ice-ocean drag coefficients from the turbulence observations. The mixed layer base was below the flux measurement depths and the majority of the melting had finished, or there was enough open water and vertical mixing that the freshwater forcing from the surface did not reside in mixed layers shallower than 6.5-m depth. The agreement between C_{d0} and C_{d6} as well as β_0 and β_6 (**Figure 12**) at first glance indicates that these estimates are appropriate. However, as shown below (Section 4.3), the drag coefficient formulation is not appropriate in September at C2 (the correlation between ice-ocean shear squared and friction velocity squared was negligible).

The ratios of wind to ice speed, and ice to ocean speed were similar between C2 and C5 despite the different ice concentrations. The Nansen number (ratio of wind to ice speed, **Figure 13g**) returned to values around 0.02 (50:1)

at C2, and remained at this level at C5, indicating that ice concentrations of 70–80% are more effective at transferring momentum to the ice than those near 10%. The ratio of ocean speed to ice speed was also indistinguishable between these two clusters (**Figure 13h**).

4.2.5 1 October – 31 December

By 1 October, the mixed layer at C5 had deepened to near 40-m depth (**Figure 9**) but did not deepen much further, and ice concentration remained above 98% during this time (with a few exceptions when ice concentration fell to around 95%). The ice-ocean drag coefficient had a median value of $C_{d6} = 4.3 \times 10^{-3}$ and did not vary significantly in time (**Figure 12**).

4.3 Under-ice roughness and Rossby similarity

One simple indicator of whether an ice-ocean drag coefficient is appropriate is the exponent, *n*, of the regression between ice-ocean shear and friction velocity squared. A drag coefficient formulation corresponds to an exponent of $n = 2$ (see Equation 5), with Rossby similarity suggesting a smaller exponent (McPhee, 2012). Least squares fitting of to $(u_{ice} - u_6)^n$ performed for each cluster and time period (March – 15 May, 16 May – 27 June, 1 September – 1 October) returned exponents significantly smaller than 2, ranging from 1.24 to 1.76 (**Table 1**). Correlation coefficients between stress and velocity difference to the power *n* at C2–C4 varied over 0.74–0.84 during the first two time periods (**Table 2**). In September, the correlation coefficient at C2 was not significantly different from zero ($r^2 = 0.24$) while that at C5 was significant ($r^2 = 0.74$), which likely results from the differences in ice concentration (less than 30% versus greater than 80%) and/or floe size (**Figure 7a** and **c**). The quadratic drag coefficient formulation ($n = 2$) corresponds to correlation coefficients that were only marginally smaller: $r^2 = 0.68$ to 0.80 during the first two time periods, while during September, $r^2 = 0.25$ at C2 and $r^2 = 0.71$ at C5 (**Table 2**). The minor differences between the variable and quadratic exponent suggest that the quadratic drag coefficient is an acceptable parameterization; however, neither is valid during September conditions at C2.

To compare with Rossby similarity theory, the ice-ocean drag coefficient was considered as a function of ice speed. The median, 25th, and 75th percentiles of C_{d0} and β_0 were estimated for different ranges of $u_{ice} - u_{geo}$ over March – 15 May and 16 May – 27 June (**Figure 15**). Significant differences in C_{d0} and to a lesser extent turning angle were observed between the clusters for the same ice speed, with differences between clusters more pronounced over 16 May – 27 June. However, in either time period and for ice speeds larger than 0.02 m s^{-1}, C_{d0} estimates within the individual C2–C4 clusters did not vary significantly with ice speed (**Figure 15a, c**). A wide range of turning angles was observed for most ice speeds, especially those less than 0.1 m s^{-1} (**Figure 15b, d**). Differences between clusters were significant over 16 May – 27 June, with the smallest turning angles at C2 (**Figure 15d**), consistent with Rossby similarity (smaller turning angle for smaller ice roughness; McPhee, 2012). While Rossby similarity can account for non-neutral buoyancy flux conditions, the lack of variation with ice speed is consistent with small ice roughness lengths (e.g., 1 mm) and neutral buoyancy flux (see **Figure 5** of McPhee, 2012; **Figure 15** of Randelhoff et al., 2014). Neutral conditions are consistent with the small observed buoyancy fluxes that corresponded to 0.2 cm day^{-1} of ice growth during March – 15 May, and 0.1 cm day^{-1} of ice melt during 16 May – 27 June.

Table 1: The exponent, *n*, ± error, of u_{*6}^2 versus $(u_{ice} - u_6)^n$. DOI: https://doi.org/10.1525/elementa.241.t1

Cluster	Mar – 15 May	16 May – 27 June	1 Sept – 1 Oct
C2	1.24 ± 0.15	1.28 ± 0.17	0.51 ± 0.55
C3	1.26 ± 0.15	1.63 ± 0.18	–[a]
C4	1.76 ± 0.17	1.35 ± 0.16	–[a]
C5	–[a]	–[a]	1.47 ± 0.29

[a]data are not available for these clusters and time periods.

Table 2: Correlation coefficient squared of u_{*6}^2 versus $(u_{ice} - u_6)^n$. DOI: https://doi.org/10.1525/elementa.241.t2

Cluster	Mar – 15 May		16 May – 27 June		1 Sept – 1 Oct	
	$n = 2$	Variable n[a]	$n = 2$	Variable n[a]	$n = 2$	Variable n[a]
C2	0.69	0.74	0.68	0.77	0.25	0.24
C3	0.68	0.75	0.79	0.83	–[b]	–[b]
C4	0.80	0.84	0.74	0.81	–[b]	–[b]
C5	–[b]	–[b]	–[b]	–[b]	0.71	0.74

[a]*n* is the value from Table 1.
[b]data are not available for these clusters and time periods.

The C_{d0} estimates were finally utilized to estimate a roughness length scale, z_0, using (8). Like the ice-ocean drag coefficient (**Figure 12**), the roughness length estimates had significant day-to-day variability but their weekly median values were more stable (**Figure 16**). The temporal and spatial variations in z_0 were similar to those of the ice-ocean drag coefficient: roughness lengths were smallest at C2 (typically less than 0.1 cm), and increased at C3 and decreased at C2 and C4 between March – 15 May and 16 May – 27 June. Some of the details of the ice roughness length differed from that of the ice-ocean drag coefficient, such as a more distinct separation of values between C3 and C4 that more clearly occurred on 15 May.

4.4 Kinetic energy budget of the ice

The final view of the air-ice-ocean system considered here is given by constructing a kinetic energy budget for the ice. Wind work and ocean work terms (Equation 9a and b) are first considered using $C_{da} = 1.5 \times 10^{-3}$ (Guest and Davidson, 1991), and a constant in time C_{d6} of 0.9×10^{-3},

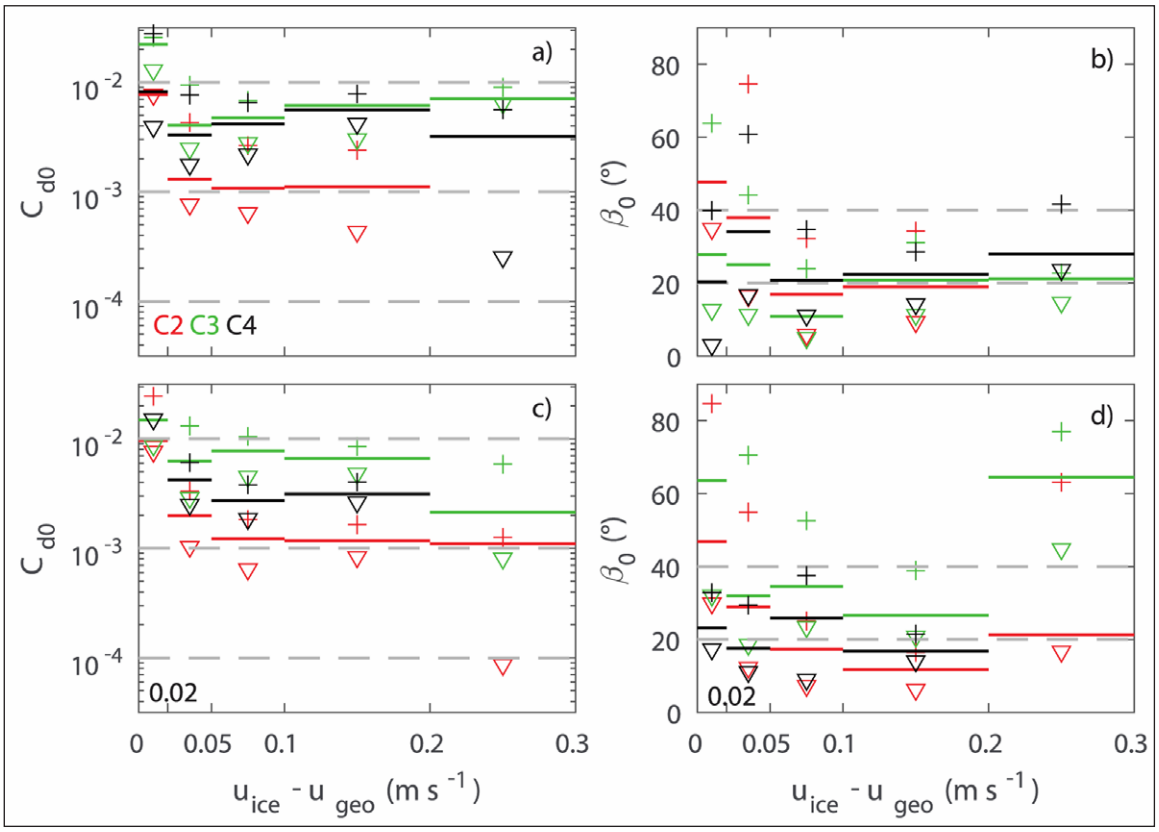

Figure 15: Statistics of the ice-ocean drag coefficient and turning angle. Median (lines), and 25th (triangles) and 75th percentiles (plus symbols) in **a)–b)** over the period of March – 15 May, and in **c)–d)** over 16 May – 27 June for daily averaged, in a) and c), ice-ocean drag coefficient (C_{d0}) and in b) and d), turning angle (β_0) as a function of ice speed relative to the geostrophic velocity. DOI: https://doi.org/10.1525/elementa.241.f15

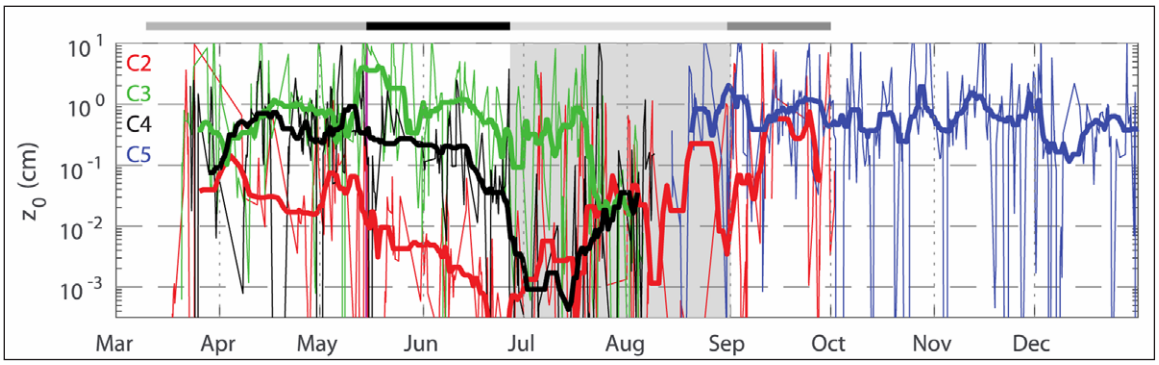

Figure 16: Time series at C2–C5 of ice roughness length estimates. The ice roughness length, z_0 (thin), and its weekly median value (thick) are shown. Daily averaged u_{*0} and velocity components referenced to u_{geo} were used. Records with $u_{*0} < 3 \times 10^{-3}$ were excluded. Gray bars, magenta line, and gray shading as in Figure 10. DOI: https://doi.org/10.1525/elementa.241.f16

3.8×10^{-3}, and 2.9×10^{-3} at C2–C4, values that derive from the median values from each cluster over March – 27 June (**Figure 12b**). At C2–C4, wind work and ocean work on the ice (Equation 9a and b) were the dominant terms controlling the kinetic energy of the ice; the time rate of change term (Equation 9c) was negligible in comparison, and the motion of the ice across a sloped sea surface (Equation 9d) was typically a factor of 10 smaller than the wind and ocean work terms (**Figure 17**). We refrain from drawing conclusions about the residual (nominally the internal ice stress plus error; not shown), because minor changes in C_{da} and C_{d6} greatly impact the magnitude of the residual and no discernable pattern was evident. Throughout the time series, wind work and ocean work were of opposing sign and largely balanced (**Figure 17a, b,** and **c**), consistent with free drift, and variable in time with elevated work corresponding to elevated ice speeds. The two terms balanced most closely at C4, with differences at C2 and C3 likely due to the invalid assumption of a spatially constant C_{da}. In most cases, wind work was positive and ocean work negative, corresponding to winds that forced ice motion that in turn forced the ocean. The two exceptions at each cluster are an event in early May, and a period of a few weeks in late July; the alignment of the wind, ice and ocean was not always that for positive wind work.

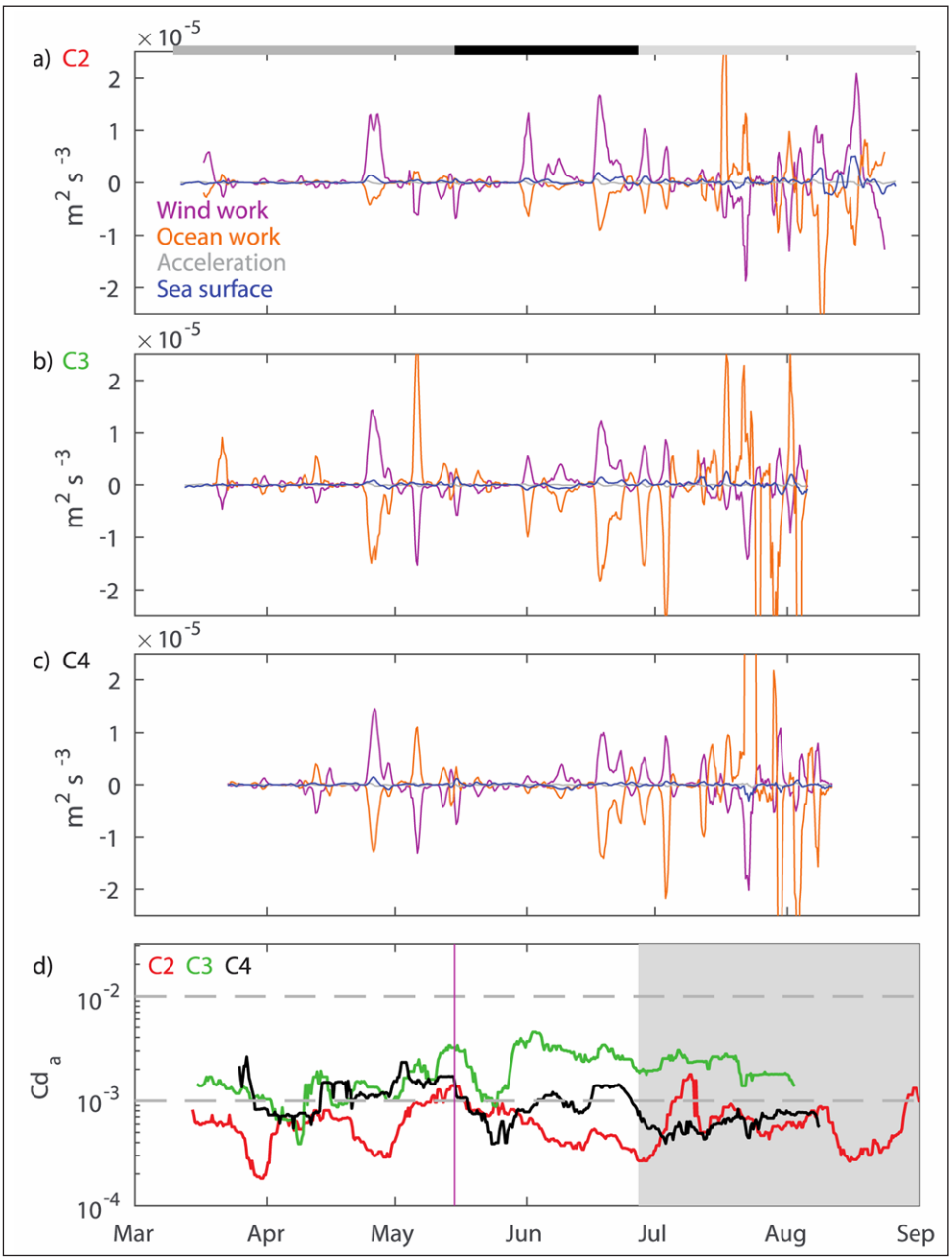

Figure 17: Kinetic energy budget of the ice. Daily averaged terms in Equation 9 include: wind work (magenta), ocean work (orange), acceleration of the ice (gray), and sea surface motion (blue) at **a)** C2, **b)** C3, and **c)** C4 using constant in time air-ice and ice-ocean drag coefficients. The ice-ocean drag coefficient varies between clusters (see text). **d)** Time series of the weekly median air-ice drag coefficient required for wind work and ocean work terms to balance. Gray bars, vertical magenta line, and shading as in Figure 10. DOI: https://doi.org/10.1525/elementa.241.f17

A temporally variable C_{da} was constructed by exactly balancing wind and ocean work using the weekly mean C_{d6} (**Figure 12b**). Not surprisingly, variation of the resulting weekly median C_{da} (**Figure 17d**) resembles that of C_{d6}; C_{da} was smallest during March – 15 May at C2, and largest during 16 May – 27 June at C3. The overall magnitude range during March – 27 June was 0.2–3.4 × 10^{-3}, essentially in agreement with previous observations in 100% ice concentration and smaller than observed in the marginal ice zone (Overland, 1985; Anderson, 1987; Guest and Davidson, 1987, 1991; Castellani et al., 2014).

5. Discussion

5.1 Momentum transfer

Spatial differences in ice-ocean drag coefficients between the clusters resulted from the specific details of the local sea ice field surrounding each cluster. Each cluster was installed within a conglomerate of MYI imbedded within FYI, with only minor differences in the percentage of MYI near each cluster (ranging between ~58% and 64%; Section 4.2.1). One major difference was the size of the MYI floes, with C2 having the largest MYI floes and those at C3 and C4 being smaller (**Figure 6**; see also Hwang et al., 2017). Contrasts between FYI and MYI thickness contribute to ice-ocean drag, such that the smaller MYI floes at C4 allowed for a greater number of contrasting 'ice edges' and an elevated ice-ocean drag coefficient compared to C2. These differences in MYI floe size translated to a factor of three spatial difference in the ice-ocean drag coefficients between clusters. Compared with the canonical ice-ocean drag coefficient of 5.5 × 10^{-3} (McPhee, 1980), ice-ocean drag coefficients were 80–85% smaller at C2 and 10–55% smaller at C3 and C4. In terms of roughness lengths, C3 and C4 were order 10 mm through 27 June, smaller than a typical MYI value of 50 mm (McPhee, 2002, 2012; Shaw et al., 2008), while the C2 roughness length was 0.1–1.0 mm, values typically associated with FYI (McPhee et al., 1999; McPhee, 2012). There is some uncertainty in the specific values of the ice-ocean drag coefficients (and roughness lengths); however, it is the relative differences spatially between clusters and temporally that matter most to the conclusions of this paper. While the clusters are referred to here in relative terms as smoother (C2) and rougher ice (C3 and C4), in an historical context, C3 and C4 are smooth ice, and C2 is very smooth ice.

The ice-ocean drag coefficient changed seasonally beginning around 15 May. At C3, the increase in ice-ocean drag on approximately 15 May can be attributed to a clump of thick, ridged MYI that transitioned to within 1 km of the cluster center during this time (**Figure 6b**; Section 4.2.1). The timing of this transition and the observed increase in the ice-ocean drag coefficient suggests that the ice-ocean drag coefficient is sensitive to large ridges within 2–3 km of turbulent stress measurement sites but not to those that are more than ~5 km away (for cases with these typical ice speeds, as the distance of influence depends on drift speed). At C2 and C4, the ice-ocean drag coefficient decreased gradually during 16 May – 27 June. The decrease began in the absence of any rearrangement of the ice, and before bottom and snow melt began or the mixed layer shoaled. Thus the decrease cannot be attributed to "slippery" mixed layers or physical smoothing of under-ice ridges. Form drag from floe edges was not influential during this time either, as indicated by the observed decrease in C_d. The decrease in ice-ocean drag was associated with an increase in daily averaged ice speed (e.g., mean ± standard deviation of 0.07 ± 0.06 m s^{-1} for March – 15 May and 0.11 ± 0.07 m s^{-1} for 16 May – 27 June at C2; **Figure 8b**) that led to an increase in ice-ocean shear without a significant change in measured friction velocity (**Figure 11**). However, the temporal decrease in C_d cannot be attributed directly to ice speed changes alone: C_d did not vary with ice speed on a daily basis, and especially at C4, values of C_d decreased between the first two time-periods for identical ice speeds (**Figure 15a** and **c**). Minor changes in ice concentration also occurred, with ice concentrations marginally lower after 15 May (mean ± standard deviation for AMSR2 values of 99.5 ± 0.8% versus 97.8 ± 4.5% at C2 and 99.4 ± 0.8% versus 97.1 ± 5.1% at C4 over March – 15 May and 16 May – 27 June, respectively). The increased ice velocity and marginally smaller ice concentration did not significantly alter the mixed layer depth, but did marginally deepen the weekly median Ekman depth at C2 where ice concentrations were lowest (from 19.4 m for March – 15 May to 23.3 m for 16 May – 27 June; **Figure 10**). In summary of all three clusters, changes in ice-ocean drag coefficients coincided with the first departures of the ice concentration from 100%, which was in turn associated with the elevated wind events (near 10 m s^{-1}) observed during late April and early May.

The measured ice velocity is representative of the larger scale of the ice floes/ice pack, but the turbulent flux observations may not be; could the decrease in ice-ocean drag over 16 May – 27 June at C2 and C4 result from this mismatch in spatial scale? A significant increase in the friction velocity averaged over the scale of the ice floe would have to result so as to balance the increase in ice speed. Such a situation could originate from ice edge effects, as suggested by several studies (Steele et al., 1989; Lu et al., 2011; Tsamados et al., 2014), but a 20–30% increase in area-averaged friction velocity seems unlikely for ice concentrations greater than 90%.

More significant changes to momentum transfer occurred in July – September. Ice to wind speed ratios in July and August were larger at C2–C4 compared with C5, despite the thicker and likely rougher ice at C5, and then decreased in September to be equivalent to values at C5, indicating that momentum was more easily transferred to the ice in moderate ice concentration conditions (**Figure 13e** and **g**). The ratio of ocean to ice speed at C2 was largest in September (**Figure 13f** and **h**), suggesting that momentum was most easily transferred to the ocean for the lowest ice concentrations (at least for smooth ice). Estimated ice-ocean drag coefficients in July – August have significant uncertainty as the turbulent flux observations were too deep relative to the thin (less than 3 m) layer of freshwater residing below the ice. Measurements to shallower depths, ideally within the logarithmic boundary layer, are needed during the melt season to confirm changes in ice-ocean drag coefficients.

Differences in turning angles were less distinct between clusters or with time. Turning angles of 20–25° are typical of multiyear ice, while those less than 15° would indicate smoother ice more typical of first-year ice conditions (McPhee, 1979, 2012). Observations in partial ice cover reported turning angles of 32–39° (McPhee et al., 1987; Randelhoff et al., 2014), which in part can be explained by the influence of shallow mixed layers (Randelhoff et al., 2014) that we note were not present in March – 27 June. The turning angles observed here, of 4–11° (for β_6) and 18–35° (for β_0), are in agreement with or smaller than values of typical multi-year ice.

Stratification influenced ocean currents throughout the IOBL. Due to the need to indirectly investigate ice-ocean momentum transfer at times of shallow mixed layers (July and August), it was not possible to directly determine what effect stratification had on ice-ocean drag parameterizations. However, it was clear that ocean velocities within the upper 10–20 m were altered by a shallower mixed layer base (**Figures 9** and **14**). After the mixed layer shoaled in July, modest ice speeds caused elevated mixed layer currents to extend to the base of the summer mixed layer (**Figure 9**), whereas prior to mixed layer shoaling, elevated currents at similar depth (10–15 m) were only observed with the strongest ice velocities. A similar amount of work done on a shallower mixed layer produced larger velocities within the mixed layer.

The kinetic energy budget of the ice showed little seasonal change. From March to September, wind work and ocean work were largely balanced, suggesting that air-ice and ice-ocean drag coefficients had similar spatial and temporal variability and are influenced by the same processes, in this case the marginal deviations of ice concentration from 100%. Wind and ocean work were elevated intermittently at times of elevated wind speeds, with little seasonal preference as strong wind events were not preferentially observed in any time period.

One question left largely unanswered by this study is: under what ice concentrations is an ice-ocean drag coefficient or under-ice roughness length parameterization valid? Periods when ice concentrations were less than 70% occurred in July and August when the turbulent flux observations were not shallow enough to address this question directly. The C2 observations in September were made when ice concentration was 13–30% (based on TerraSAR-X imagery) with small broken floes observed about the cluster throughout the month (e.g., **Figure 7**). An ice-ocean drag coefficient formulation was not applicable in these conditions (**Table 1**), although that conclusion is based on a small number of data points. Recent ship-based studies in summer (e.g., Randelhoff et al., 2014) find an ice-ocean drag coefficient is applicable, but for larger ice floes (~500 m), suggesting that floe size together with ice concentration will determine the applicability of an ice-ocean drag coefficient or roughness length parameterization.

It is difficult to compare the seasonal cycle of ice-ocean drag (**Figure 12**) or the inferred increase in momentum transfer in the summer (**Figure 13**) to past studies. The summer increase in ice velocity is well documented (e.g., Rampal et al., 2009), but the increase in mixed layer ocean velocities during summer can only be compared with studies on decadal and basin scales (e.g., McPhee, 2013; Armitage et al., 2017), which show an increase in mixed layer currents as the ice cover and wind forcing changed on a decadal scale. Temporal changes in ice-ocean drag and roughness have focused on its dependence on ice speed or thermodynamic forcing (e.g., McPhee, 2002; Shaw et al., 2008; Randelhoff et al., 2014), and there are no prior observations of changes in drag due to changing ice concentration. Modeling studies show that including the effects of drag from floe edges leads to a seasonal increase in the ice-ocean drag coefficient in summer (Steele et al., 1989; Tsamados et al., 2014), the opposite of what was observed here during the beginning of the ice break up. Martin et al., (2014) found an optimal ice concentration for momentum transfer (maximum τ) near 80%. Our observations do not indicate clearly if there is a preferred ice concentration for maximum stress, but the maximum Nansen numbers observed at moderate ice concentrations (**Figure 13a, c, e,** and **g**) support the concept of maximum momentum transfer to the ice (but not necessarily the ocean) for moderate ice concentration. Comparisons with such modeling studies are imperfect as such studies address the entire Arctic domain (Martin et al., 2014; Tsamados et al., 2014), and may neglect other seasonal changes to the system such as mixed layer properties (Tsamados et al., 2014) or ice roughness (Martin et al., 2014).

5.2 Implications for numerical modeling

An important consideration is how these observations from MIZ instrument clusters scale up to the size of a grid cell in a numerical model. The rearrangement of the ice in early May at C3 shows that the ice-ocean drag coefficient estimates provided by direct covariance flux estimates are sensitive to ice conditions within a 2–3 km distance of the measurement site (see Section 5.1). For a more uniform distribution of ice types, such as at C2 and C4 (**Figure 6**), the observed estimates may be sensitive to roughness features over a slightly larger area (e.g., 5 km), and so representative of the wider region over which the ice type distribution is uniform (at least 30 km at C2 and C4). Temporal and spatial variations in the ice-ocean drag at least as large as those observed here (a factor of three spatially, and at least 20–30% temporally) should be included in numerical models with 1–10 km grid cells, which are becoming more common. For models with larger grid cells (e.g., 30–60 km or larger), a constant ice-ocean drag coefficient for larger ice concentrations may be appropriate. The rearrangement of the individual pieces of the ice pack, such as those observed at C3, may not be relevant to a 30–60 km scale (although the breakup of such MYI floes is relevant). It is the rougher pieces of ice within the 30–60 km grid cell that will determine the area-averaged ice-ocean drag coefficient.

Like the ITP-V and AOFB instruments utilized in this study, a numerical model uses a fixed depth for its shallowest grid-point that for some models is likely deeper than the 1–2 m buoyant surface layers observed in summer,

equivalent to trusting our ice-ocean drag coefficient estimates in July and August. The C_{d0} and C_{d6} estimates in July – August are inaccurate, and show that a constant C_d assumption is not valid. Explicit resolution of the ephemeral mixed layers is required for accurate modeling of the air-ice-ocean system.

These observations also have implications for whether an ice-ocean drag coefficient that depends on ice age, ice thickness, or ice concentration is appropriate. Under full ice cover, the influence of the MYI patch at C3 suggests that ice type/age/thickness is a controlling factor with rougher patches dominating the area-averaged C_d. With low ice concentrations, ice type/age/thickness may be less influential than floe size or the presence of shallow, "slippery" mixed layers. A single parameterization, e.g., based on ice age or thickness, will likely not suit all of these varying conditions (what is suitable at 90% ice concentration will not be suitable at 10% ice concentration).

5.3 Implications for a changing Arctic

On the decadal scale, some conclusions can be drawn about the net effects of changes in ice concentration and ice topography on the air-ice-ocean system. Ice concentration is a controlling factor of the ice to wind speed ratio and the ocean to ice speed ratio (**Figure 13**); our results suggest that both ice speed and surface ocean current speed will increase as moderate to lower ice concentrations become spatially or temporally more common. However, smoother ice was associated with a lower ocean to ice speed ratio, suggesting that surface ocean speeds will decrease if ice becomes smoother. Taken together, the MIZ observations indicate that smoother ice did not outweigh the effects of low ice concentration: the smoothest ice (C2) still showed increased ocean to ice speed ratios in moderate ice concentration conditions. This finding suggests that surface ocean velocity could become increasingly seasonal, with weaker speeds in winter under full ice cover due to smoother ice, and stronger speeds in summer due to more prevalent partial ice cover.

Changes to ice roughness and stratification will also influence the ocean's response to storm events, with more energetic currents occurring beneath rougher ice and especially with shallower stratification. On a decadal timescale, smoother ice would limit the influence of increased wind speed or increased storm activity or intensity, while more prevalent shallower mixed layers would amplify it.

An additional key factor for the air-ice-ocean system is the relative direction of the wind, ice, and ocean velocities. The relative direction between the wind and ice varied seasonally in association with the seasonal increase in ice speed and decrease in ice concentration (**Figure 14**). The relative direction between the ice and ocean velocity was influenced by ice topography, suggesting that larger differences in direction will become more common with decreasing ice roughness. Together with the rapid decay of ocean velocity with depth in the presence of shallow stratification, such changes on decadal scales could affect the accumulation or export of freshwater and sea ice from the Arctic Ocean.

6. Summary and conclusions

Observations of wind, ice, and ocean velocity together with turbulent momentum flux that spanned the melt season were used to quantify changes to momentum transfer within the air-ice-ocean system associated with the seasonally varying ice topography and concentration, and ocean stratification. The primary scientific findings from this work may be summarized as follows:

1. Ice-ocean drag coefficients and roughness lengths decreased by 20–30% in early spring, initiated by wind events and the first decrease in ice concentration from 100% (**Figures 12** and **16**). Spatial variations of a factor of three between instrument clusters (**Figures 12, 15,** and **16**) were attributable to differences in the floe sizes of MYI within the early spring fully ice-covered FYI-MYI conglomerate (**Figure 6**). Larger MYI floe sizes were associated with smoother ice and smaller ice-ocean drag coefficients.
2. An ice-ocean drag coefficient formulation was judged to be not applicable in low ice concentration conditions (~10–30%) with small floe sizes (**Figure 7**), as evidenced by low correlation between (u_*^2) and $(u_{ice} - u_6)^n$ (**Table 2**).
3. Ice speeds were largest relative to wind speeds for moderate ice concentrations (~70–90%), with full ice cover and low ice concentrations (~10–30%) as well as the different ice topographies/roughnesses having a similar ratio of ice to wind speed (**Figure 13a, c,** and **e**). Wind work and ocean work on the ice were, to first order, balanced throughout the melt season with similar spatial and temporal variations inferred in the air-ice and ice-ocean drag coefficients (**Figure 17**).
4. Ocean speeds increased relative to ice speeds as ice-ocean drag coefficients increased, and for shallow stratification conditions (**Figures 9** and **15b, d,** and **f**). Ice topography and stratification affected Ekman veering (**Figure 14**) and the depth to which wind events accelerate ocean currents (**Figure 9**).

These findings and the conclusions drawn from them are relevant to understanding the daily to decadal evolution of the ice-ocean system, but are limited with respect to the influence of shallow stratification. This limitation is due in part to shallow stratification associated with lower ice concentrations, where discerning their separate effects was not always possible. Other limitations are due to the ITP-V, which does not currently operate within a few meters of the seasonally evolving ice cover. Most importantly, turbulent flux observations at a fixed depth are insufficient for year-round observations; if placed to operate 1 m below the winter ice-ocean interface, sensors will not be shallow enough to capture the 1–2 m thick freshwater layers in summer (after 1–2 m of basal ice melt). This limitation affects all platforms with fixed depth observations that extend for several months.

The conclusions and implications of this study were only possible through the combined use of a variety of sensors and platforms and contemporaneous remote sensing observations. The targeted remote sensing observations (**Figures 6** and **7**) made it possible to: 1) pinpoint the origin of temporal changes in the ice-ocean drag coefficient to the movement of specific patches of ice, ultimately induced by a few wind events in early spring; 2) demonstrate that observations from the instrument clusters never occurred in open water conditions, even though widely used ice concentration products (e.g., AMSR2) indicated otherwise; and 3) show that the details of the FYI–MYI conglomerate, specifically MYI floe size, governed ice-ocean momentum transfer. The timing of melt pond drainage, required to correctly interpret our turbulent momentum flux observations, also derived in part from targeted remote sensing observations as well as photographic observations (e.g., Gallaher et al., 2016). The joint analysis of ITP-V, AOFB, IMB, and wind velocity data allowed several key avenues of inquiry to be investigated, including the kinetic energy budget of the ice and parameterizations of the ice-ocean drag coefficient.

This analysis has also indicated several topics for future study. The implication for an increasingly seasonal Arctic system with ice and ocean velocities that become weaker in winter and stronger in summer reinforces the importance of observing and accurately modeling changes in ice concentration and roughness on decadal and seasonal timescales. Quantifying the effects of spatially and temporally varying drag coefficients in high resolution models is also of interest. Further investigation of small ice floes in low ice concentration conditions would be useful to determine the ice concentration and/or floe size conditions under which ice-ocean drag coefficient or ice roughness parameterizations are appropriate. While some conclusions were made regarding the role of shallow stratification, further study is needed to determine possible feedbacks between changing stratification on decadal and seasonal timescales and the dynamic coupling of the ice-ocean system. Continued investigation of the ice-ocean boundary layer is warranted due to the changing Arctic environment and because parameterizations of the air-ice-ocean system required to model this environment are dependent on the grid size of interest.

Appendix A: List of symbols

C_d Ice-ocean drag coefficient
C_{da} Air-ice drag coefficient
C_{d0} Ice-ocean drag coefficient with a reference velocity 2 m above the mixed layer base
C_{d6} Ice-ocean drag coefficient with a reference velocity at ~6.5 m depth
D_E Ekman depth
h_{BL} Thickness of the ice-ocean boundary layer
h_{ice} Thickness of the ice
u Ocean velocity (from profile observations)
u_a Wind velocity
u_{geo} Ocean velocity 2 m above the mixed layer base
u_{ice} Ice velocity
u_{ref} Reference velocity
u_0 Ocean velocity extrapolated to the top of the Ekman layer
u_6 Ocean velocity (from fixed depth observations) at ~ 6.5 m depth
u_{*0} Turbulent momentum flux extrapolated to the top of the Ekman layer
u_{*4} Turbulent momentum flux observed at ~4.5-m depth (AOFB)
u_{*6} Turbulent momentum flux observed at ~6.5-m depth (ITP-V)
z_0 Under-ice roughness length
z_{ice} Ice draft
z_m Distance from the measurement depth to the ice-ocean interface
β Turning angle between the referenced ice velocity and u_0
β_0 Turning angle between the referenced ice velocity and u_0 using a reference velocity 2 m above the mixed layer base
β_6 Turning angle between the referenced ice velocity and u_0 using a reference velocity at ~6.5-m depth
κ von Kármán's constant (0.4)
η Sea surface height
ρ_a Density of the air
ρ_{ice} Density of the ice
ρ_0 Density of the ocean
τ Ice-ocean stress

Appendix B: Processing of ITP-V velocity data

The processing of velocity data from the ITP-V is detailed in Cole et al., (2015), including a discussion of error sources. In short, sensor data from the underwater profiler (while it profiles or samples at fixed depth) are used to estimate the ocean velocity relative to the (moving) ice floe supporting the system, and account for the motion of the vehicle along a potentially inclined tether. Absolute ocean velocity data are obtained by adding the estimated ice velocity. One key update was implemented here for all ITP-V systems: ice velocity was allowed to be variable in time throughout each 20–40 minute profile and fixed depth record. Ice velocity was linearly interpolated to the times of each 1-m bin (approximately 4 seconds apart in time) for each profile or each second for fixed depth profiles from the 1-hour record of ice velocity derived from GPS locations of the surface buoy. While this linear interpolation scheme could be improved upon, it was sufficient for these purposes and more accurate than assuming a constant ice velocity throughout each profile or fixed depth record. In addition, post-deployment calibration parameters for ITP-80 at C5 were updated to pitch, roll, and heading offsets of 1°, 0°, and −15°, respectively, and a radius associated with the angular velocity correction of 27.0 cm was derived and applied. All other aspects of the processing were identical to that described in Cole et al., (2015).

Data Accessibility Statement

The Ice-Tethered Profiler data can be found on the ITP program webpage (http://www.whoi.edu/itp/data). IceBridge data utilized in this study is available via

https://nsidc.org/data/ilatm1b/ (ATM data), http://nsidc.org/data/iodms1b (DMS data) and https://nsidc.org/data/docs/daac/icebridge/evaluation_products/sea-ice-freeboard-snowdepth-thickness-quicklook-index.html (quicklook ice roughness data). Other MIZ experiment data were consolidated and made available on the MIZ project website (http://www.apl.washington.edu/project/project.php?id=miz).

Acknowledgements

We gratefully acknowledge Rick Krishfield, those who assisted with the ice camp and *R/V Araon* deployments of the ITP-Vs and other instruments, and the support of the Beaufort Gyre Observing System and Joint Ocean Ice Studies cruise on the *CCGC Louis St. Laurent* for recovering ITP-77 and 79. We would also like to thank the NASA operation IceBridge and ESA CryoVex science teams for coordination of IceBridge and AEM surveys over C2. We also acknowledge the Center for Southeastern Tropical Advanced Remote Sensing for the downlink and processing of RADARSAT-2 data.

Funding information

The deployment of the ITP-Vs and the subsequent analysis effort was supported by the Office of Naval Research under grants N00014-12-10140 and N00014-12-10799.

Competing interests

The authors have no competing interests to declare.

Author contributions

- Contributed to conception and design: SC, JT
- Contributed to acquisition of data: SC, JT, MLT, SG, TS, WS, BH, TM, JW, HG, LR, SF, JR-M, CH
- Contributed to analysis and interpretation of data: SC, JT, RL, SG, TS, WS, BH, TM, JW, MO, HG, LR, AP, SF, CH
- Drafted and/or revised the article: SC, JT, MLT, SG, TS, WS, BH, TIM, JW, MO, AP, SF, CH
- Approved the submitted version for publication: SC, JT, RL, MLT, SG, TS, WS, BH, TM, JW, MO, HG, LR, AP, SF, JR-M, CH

References

Anderson, RJ 1987 Wind stress measurements over rough ice during the 1984 Marginal Ice Zone Experiment. *J Geophys Res*, **92**: 6933–6941. DOI: https://doi.org/10.1029/JC092iC07p06933

Armitage, TWK, Bacon, S, Ridout, AL, Petty, AA, Wolbach, S, et al. 2017 Arctic Ocean geostrophic circulation 2003–2014. *Cryosphere Discuss*, in review. DOI: https://doi.org/10.5194/tc-2017-22

Arntsen, AE, Song, AJ, Perovich, DK and **Richter-Menge, JA** 2015 Observations of the summer breakup of an Arctic sea ice cover. *Geophys Res Lett*, **42**: 8057–8063. DOI: https://doi.org/10.1002/2015GL065224

Beckers, JF, Haas, C, Elder, B, Hiemstra, C, Tilling, R, et al. 2015 CryoVEx2014 – In-situ measurements at MIZ/ONR and NORD (Greenland) ice camps. ESA Ground Team Report. ESA contract 4000110552/14/MP/vb, 46.

Castellani, G, Lüpkes, C, Hendricks, S and **Gerdes, R** 2014 Variability of Arctic sea-ice topography and its impacts on the atmospheric surface drag. *J Geophys Res*, **119**: 6743–6762. DOI: https://doi.org/10.1002/2013JC009712

Cavalieri, DJ and **Parkinson, CL** 2012 Arctic sea ice variability and trends, 1979–2010. *Cryosphere*, **6**: 881–889. DOI: https://doi.org/10.5194/tc-6-881-2012

Cole, ST, Thwaites, FT, Krishfield, RA and **Toole, JM** 2015 Processing of velocity observations from Ice-Tethered Profilers. *Proc MTS/IEEE Oceans' 2015*, 1–10. Washington DC.

Cole, ST, Timmermans, M-L, Toole, JM, Krishfield, RA and **Thwaites, FT** 2014 Ekman veering, internal waves, and turbulence observed under Arctic sea ice. *J Phys Oceanogr*, **44**: 1306–1328. DOI: https://doi.org/10.1175/JPO-D-12-0191.1

Comiso, JC 2012 Large decadal decline of the Arctic multiyear ice cover. *J Climate*, **25**: 1176–1193. DOI: https://doi.org/10.1175/JCLI-D-11-00113.1

Dee, DP, Uppala, SM, Simmons, AJ, Berrisford, P, Poli, P, et al. 2011 The ERA-Interim reanalysis: configuration and performance of the data assimilation system. *Q J R Meteorol Soc*, **137**: 553–597. DOI: https://doi.org/10.1002/qj.828

Ekman, VW 1905 On the influence of the earth's rotation on ocean-currents. *Ark Mat, Astron Fys*, **2**: 1–52.

Fer, I, Skogseth, R and **Geyer, F** 2010 Internal waves and mixing in the Marginal Ice Zone near the Yermak Plateau. *J Phys Oceanogr*, **40**: 1613–1630. DOI: https://doi.org/10.1175/2010JPO4371.1

Fer, I and **Sundfjord, A** 2007 Observations of upper ocean boundary layer dynamics in the marginal ice zone. *J Geophys Res*, **112**(C04): 012. DOI: https://doi.org/10.1029/2005JC003428

Gallaher, SG, Stanton, TP, Shaw, WJ, Cole, ST, Toole, JM, et al. 2016 Evolution of a Canada Basin ice-ocean boundary layer and mixed layer across a developing thermodynamically forced marginal ice zone. *J Geophys Res*, **121**: 6223–6250. DOI: https://doi.org/10.1002/2016JC011778

Guest, PS and **Davidson, KL** 1987 The effect of observed ice conditions on the drag coefficient in the summer East Greenland Sea marginal ice zone. *J Geophys Res*, **92**: 6943–6954. DOI: https://doi.org/10.1029/JC092iC07p06943

Guest, PS and **Davidson, KL** 1991 The aerodynamic roughness of different types of sea ice. *J Geophys Res*, **96**: 4709–4721. DOI: https://doi.org/10.1029/90JC02261

Haas, C, Hendricks, S, Eicken, H and **Herber, A** 2010 Synoptic airborne thickness surveys reveal state of Arctic sea ice cover. *Geophys Res Lett*, **37**(L09): 501. DOI: https://doi.org/10.1029/2010GL042652

Hwang, B, Wilkinson, J, Maksym, T, Graber, HC, Schweiger, A, et al. 2017 Winter-to-summer transition of Arctic sea ice breakup and floe size distribution in the Beaufort Sea. *Elementa Sci Anth, accepted*. DOI: https://doi.org/10.1525/elementa.232

Jackson, K, Wilkinson, J, Maksym, T, Meldrum, D, Beckers, J, et al. 2013 A novel and low-cost sea ice mass balance buoy. *J Atmos Oceanic Technol*, **30**: 2676–2688. DOI: https://doi.org/10.1175/JTECH-D-13-00058.1

Johannessen, OM, Johannessen, JA, Morison, J, Farrelly, BA and **Svendsen, EAS** 1983 Oceanographic conditions in the Marginal ice Zone north of Svalbard in early fall 1979 with an emphasis on mesoscale processes. *J Geophys Res*, **88**: 2755–2769. DOI: https://doi.org/10.1029/JC088iC05p02755

Koenig, L, Martin, S, Studinger, M and **Sonntag, J** 2010 Polar Airborne Observations Fill Gap in Satellite Data. *Eos Trans AGU*, **91**: 333–334. DOI: https://doi.org/10.1029/2010EO380002

Krabill, WB, Abdalati, W, Frederick, E, Manizade, S, Martin, C, et al. 2002 Aircraft laser altimetry measurement of elevation changes of the green land ice sheet: technique and accuracy assessment. *J Geodynam*, **34**: 357–376. DOI: https://doi.org/10.1016/S0264-3707(02)00040-6

Krishfield, R, Proshutinsky, A, Tateyama, K, Williams, WM, Carmack, EC, et al. 2014 Deterioration of perennial sea ice in the Beaufort Gyre from 2003 to 2012 and its impact on the oceanic freshwater cycle. *J Geophys Res*, **119**: 1271–1305. DOI: https://doi.org/10.1002/2013JC008999

Krishfield, R, Toole, J, Proshutinsky, A and **Timmermans, M-L** 2008a Automated Ice-tethered Profilers for seawater observations under pack ice in all seasons. *J Atmos Oceanic Technol*, **25**: 2091–2105. DOI: https://doi.org/10.1175/2008JTECHO587.1

Krishfield, R, Toole, J and **Timmermans, M-L** 2008b ITP data processing procedures. Woods Hole Oceanographic Institution Tech. Rep., 24 Available at: http://www.whoi.edu/fileserver.do?id=35803&pt=2&p=41486.

Kudryavtsev, VN and **Soloviev, AV** 1990 Slippery near-surface layer of the ocean arising due to daytime solar heating. *J Phys Oceanogr*, **20**: 617–628. DOI: https://doi.org/10.1175/1520-0485(1990)020<0617:SNSLOT>2.0.CO;2

Kwok, R, Cunningham, GF, Wensnahan, M, Rigor, I, Zwally, HJ, et al. 2009 Thinning and volume loss of the Arctic Ocean sea ice cover: 2003–2008. *J Geophys Res*, **114**(C07): 005. DOI: https://doi.org/10.1029/2009JC005312

Kwok, R, Spreen, G and **Pang, S** 2013 Arctic sea ice circulation and drift speed: Decadal trends and ocean currents. *J Geophys Res*, **118**: 2408–2425. DOI: https://doi.org/10.1002/jgrc.20191

Lee, CM, Cole, S, Doble, M, Freitag, L, Hwang, B, et al. 2012 Marginal Ice Zone (MIZ) program: Science and experiment plan. Tech. Rep. APL-UW 1201, 48. *Appl. Phys. Lab.*, Univ. of Wash., Seattle, Wash.

Leppäranta, M 2011 The Drift of Sea Ice, (Second Edition), Springer Heidelberg Dordrecht London New York, 347. DOI: https://doi.org/10.1007/978-3-642-04683-4

Lu, P, Li, Z, Cheng, B and **Leppäranta, M** 2011 A parameterization of the ice–ocean drag coefficient. *J Geophys Res*, **116**(C07): 019. DOI: https://doi.org/10.1029/2010JC006878

Martin, T, Steele, M and **Zhang, J** 2014 Seasonality and long-term trend of Arctic Ocean surface stress in a model. *J Geophys Res*, **119**: 1723–1738. DOI: https://doi.org/10.1002/2013JC009425

Martin, T, Tsamados, M, Schroeder, D and **Feltham, DL** 2016 The impact of variable sea ice roughness on changes in Arctic Ocean surface stress: A model study. *J Geophys Res*, **121**: 1931–1952. DOI: https://doi.org/10.1002/2015JC011186

Maykut, GA and **McPhee, MG** 1995 Solar heating of the Arctic mixed layer. *J Geophys Res*, **100**: 24691–24703.

McPhee, MG 1978 A simulation of inertial oscillation in drifting pack ice. *Dyn Atmos Oceans*, **2**: 107–122. DOI: https://doi.org/10.1016/0377-0265(78)90005-2

McPhee, MG 1979 The effect of the oceanic boundary layer on the mean drift of pack ice: Application of a simple model. *J Phys Oceanogr*, **9**: 388–400. DOI: https://doi.org/10.1175/1520-0485(1979)009<0388:TEOTOB>2.0.CO;2

McPhee, MG 1980 An analysis of pack ice drift in summer. In: Pritchard, R (ed.), *Sea ice processes and models*, 62–75. University of Washington Press, Seattle.

McPhee, MG 2002 Turbulent stress at the ice/ocean interface and bottom surface hydraulic roughness during the SHEBA drift. *J Geophys Res*, **107**: 8037. DOI: https://doi.org/10.1029/2000JC000633

McPhee, MG 2008 *Air-ice-ocean interaction: Turbulent ocean boundary layer exchange processes*, 226. Springer.

McPhee, MG 2012 Advances in understanding ice–ocean stress during and since AIDJEX. *Cold Reg Sci Technol*, **76–77**: 24–36. DOI: https://doi.org/10.1016/j.coldregions.2011.05.001

McPhee, MG 2013 Intensification of geostrophic currents in the Canada Basin, Arctic Ocean. *J Climate*, **26**: 3130–3138. DOI: https://doi.org/10.1175/JCLI-D-12-00289.1

McPhee, MG, Kottmeier, C and **Morison, JH** 1999 Ocean heat flux in the central Weddell Sea during winter. *J Phys Oceanogr*, **29**: 1166–1179. DOI: https://doi.org/10.1175/1520-0485(1999)029<1166:OHFITC>2.0.CO;2

McPhee, MG, Maykut, GA and **Morison, JH** 1987 Dynamics and thermodynamics of the ice/upper ocean system in the marginal ice zone of the Greenland Sea. *J Geophys Res*, **92**: 7017–7031. DOI: https://doi.org/10.1029/JC092iC07p07017

Ortiz, MD 2017 Remote sensing of open water fraction and melt ponds in the Beaufort Sea using machine learning algorithms, U. Miami, Open Access Dissertations.

Overland, JE 1985 Atmospheric boundary layer structure and drag coefficients over sea ice. *J Geophys Res*, **90**: 9029–9049. DOI: https://doi.org/10.1029/JC090iC05p09029

Peralta-Ferriz, C and **Woodgate, R** 2015 Seasonal and interannual variability of pan-Arctic surface

mixed layer properties from 1979 to 2012 from hydrographic data, and the dominance of stratification for multiyear mixed layer depth shoaling. *Prog Oceanogr*, **134**: 19–53. DOI: https://doi.org/10.1016/j.pocean.2014.12.005

Petty, AA, Tsamados, MC, Kurtz, NT, Farrell, SL, Newman, T, et al. 2016 Characterizing Arctic sea ice topography using high-resolution IceBridge data. *Cryosphere*, **10**: 1161–1179. DOI: https://doi.org/10.5194/tc-10-1161-2016

Pinkel, R 2005 Near-inertial wave propagation in the western Arctic. *J Phys Oceanogr*, **35**: 645–665. DOI: https://doi.org/10.1175/JPO2715.1

Rampal, P, Weiss, J and **Marsan, D** 2009 Positive trend in the mean speed and deformation rate of Arctic sea ice, 1979–2007. *J Geophys Res*, **114**(C05): 013. DOI: https://doi.org/10.1029/2008JC005066

Randelhoff, A, Sundfjord, A and **Renner, AHH** 2014 Effects of a shallow pycnocline and surface meltwater on sea ice-ocean drag and turbulent heat flux. *J Phys Oceanogr*, **44**: 2176–2190. DOI: https://doi.org/10.1175/JPO-D-13-0231.1

Shaw, WJ, Stanton, TP, McPhee, MG and **Kikuchi, T** 2008 Estimates of surface roughness length in heterogeneous under-ice boundary layers. *J Geophys Res*, **113**(C06): 012. DOI: https://doi.org/10.1029/2007JC004550

Shirasawa, K and **Ingram, RG** 1991 Characteristics of the turbulent oceanic boundary layer under sea ice. Part 1: A review of the ice–ocean boundary layer. *J Mar Syst*, **2**: 153–160. DOI: https://doi.org/10.1016/0924-7963(91)90021-L

Sirevaag, A, de la Rosa, S, Fer, I, Nicolaus, M, Tjernstrom, M, et al. 2011 Mixing, heat fluxes and heat content evolution of the Arctic Ocean mixed layer. *Ocean Sci*, **7**: 335–349. DOI: https://doi.org/10.5194/os-7-335-2011

Spreen, G, Kaleschke, L and **Heygster, G** 2008 Sea ice remote sensing using AMSR-E 89 GHz channels. *J Geophys Res*, **113**(C02): S03. DOI: https://doi.org/10.1029/2005JC003384

Steele, M, Morison, JH and **Untersteiner, N** 1989 The partition of air-ice-ocean momentum exchanges as a function of ice concentration, floe size, and draft. *J Geophys Res*, **94**: 12738–12750. DOI: https://doi.org/10.1029/JC094iC09p12739

Sundfjord, A, Fer, I, Kasajima, Y and **Svendsen, H** 2007 Observations of turbulent mixing and hydrography in the marginal ice zone of the Barents Sea. *J Geophys Res*, **112**(C05): 008. DOI: https://doi.org/10.1029/2006JC003524

Thwaites, FT and **Krishfield, R** 2013 Development of a second-generation Ice Tethered Profiler with velocity sensor. *Proc Oceans 2013 San Diego Conference*, San Diego, CA, IEEE Xplore.

Toole, JM, Krishfield, RA, Timmermans, M-L and **Proshutinsky, A** 2011 The Ice-Tethered Profiler: Argo of the Arctic. *Oceaongr*, **24**: 126–135. DOI: https://doi.org/10.5670/oceanog.2011.64

Tsamados, M, Feltham, D, Schroeder, D, Flocco, D, Farrell, SL, et al. 2014 Impact of variable atmospheric and oceanic form drag on simulations of Arctic sea ice. *J Phys Oceanogr*, **44**: 1329–1353. DOI: https://doi.org/10.1175/JPO-D-13-0215.1

Williams, AJ, Thwaites, FT, Morrison, AT, Toole, JM and **Krishfield, R** 2010 Motion tracking in an acoustic point-measurement current meter. *Proc. OCEANS 2010 IEEE*, 1–8. Sydney, Australia, IEEE. DOI: https://doi.org/10.1109/OCEANSSYD.2010.5603862

Zhao, M, Timmermans, M-L, Cole, S, Krishfield, R, Proshutinsky, A, et al. 2014 Characterizing the eddy field in the Arctic Ocean halocline. *J Geophys Res*, **119**: 8800–8817. DOI: https://doi.org/10.1002/2014JC010488

How to cite this article: Cole, ST, Toole, JM, Lele, R, Timmermans, M-L, Gallaher, SG, Stanton, TP, Shaw, WJ, Hwang, B, Maksym, T, Wilkinson, JP, Ortiz, M, Graber, H, Rainville, L, Petty, AA, Farrell, SL, Richter-Menge, JA and Haas, C 2017 Ice and ocean velocity in the Arctic marginal ice zone: Ice roughness and momentum transfer. *Elem Sci Anth,* 5: 55, DOI: https://doi.org/10.1525/elementa.241

Domain Editor-in-Chief: Jody W. Deming, University of Washington, US

Guest Editor: James Thomson, University of Washington, US

Knowledge Domain: Ocean Science

Part of an *Elementa* Special Feature: Marginal Ice Zone Processes in the Summertime Arctic

Submitted: 01 February 2017 **Accepted:** 21 July 2017 **Published:** 21 September 2017

Copyright: © 2017 The Author(s). This is an open-access article distributed under the terms of the Creative Commons Attribution 4.0 International License (CC-BY 4.0), which permits unrestricted use, distribution, and reproduction in any medium, provided the original author and source are credited. See http://creativecommons.org/licenses/by/4.0/.

ELEMENTA Science of the Anthropocene

Elem Sci Anth is a peer-reviewed open access journal published by University of California Press.

OPEN ACCESS